

Copyright
by
Aale R. Naqvi
2010

**The Thesis Committee for Aale R. Naqvi
Certifies that this is the approved version of the following thesis:**

**Investigation of Doppler Features Resulting from Wind Turbine
Scattering**

**APPROVED BY
SUPERVISING COMMITTEE:**

Supervisor:

Hao Ling, Supervisor

Andrea Alu

**Investigation of Doppler Features Resulting from Wind Turbine
Scattering**

by

Aale R. Naqvi, B.S.

Thesis

Presented to the Faculty of the Graduate School of

The University of Texas at Austin

in Partial Fulfillment

of the Requirements

for the Degree of

Master of Science in Engineering

The University of Texas at Austin

December 2010

Acknowledgements

I am very much thankful to my advisor, Dr. Ling, for guiding me in carrying out this work. I have immensely benefitted from his keen insights and encouragement without which this work would not have been possible. I would like to thank my colleagues for helping me with laboratory measurements and useful discussions. I am also very grateful to Dr. Alu for being my Reader. Finally, I would like to thank my family for all their support.

December 2010

Abstract

Investigation of Doppler Features Resulting from Wind Turbine Scattering

Aale Naqvi, M.S.E

The University of Texas at Austin, 2010

Supervisor: Hao Ling

The rapid growth in the number of large wind farms has raised serious concerns about their effects on existing radar systems. The large size and rotational movement of the turbine blades can give rise to significant Doppler clutters, which interfere with the detection of moving targets such as aircraft and storms. A previous Air Force study has collected and analyzed the time-varying radar cross section resulting from the blade rotation of a single 1.5 MW turbine. However, multiple interactions taking place in a turbine were not studied in detail. Multiple interactions could play an important role in the propagation of radar signals through wind farms.

This thesis sets out to more closely examine the various Doppler features resulting from the scattering due to a single turbine. Backscattered and forward scattered data are measured at Ku-band from various wind turbine models using a motorized turntable in

the laboratory. The tested models include a 1:160 scale model turbine, a 3-arm wire model turbine, and a small wind turbine from Bergey Windpower with 2' blades. The data are processed based on the short-time Fourier transform in order to relate the resulting time-varying Doppler features to various scattering mechanisms. The experimental findings are corroborated by simulations performed using the Numerical Electromagnetics Code (NEC). Furthermore, we propose a post-processing general method to reduce the intensity of the turbine scattered data. This method is applied to filter out simulated Doppler clutter from two different simulation techniques. First, the method is applied to remove the simulated Doppler clutter from the point scatterer model. Next, the algorithm is applied to simulated backscattered data generated using a high-frequency ray tracing code, Ahilo.

Table of Contents

List of Figures	viii
Chapter 1 Introduction.....	01
Chapter 2 Multiple Scattering Studies on Scaled Turbine Models	04
2.1 Methodology	04
2.2 Doppler Feature Analysis	07
2.2.1 The 1:160 Scaled Model	07
2.2.2 3-Arm Model	11
2.2.3 Bergey Windpower Turbine	18
2.3 Moving Target the 3-Arm Wire Model	22
Chapter 3 A Signal Filtering Technique to Remove Doppler Clutters Caused by Wind Turbines	26
3.1 Point Scatterer Model	27
3.2 Basis Parameterization.....	30
3.3 Simulations.....	32
3.3.1 Basis Parameterization Applied to Point Scatterer Data.....	32
3.3.2 Backscattered Data Generated Using Ahilo	38
3.3.3 Basis Parameterization Applied to Ahilo Data.....	41
Chapter 4 Conclusions.....	46
Bibliography	47

List of Figures

Figure 2.1:	Graphical illustration of the discrete short time Fourier transform .	06
Figure 2.2:	1:160 scaled model turbine measurements. (a) Photo of the model turbine. (b) Backscattered spectrogram after STFT processing.	08
.Figure 2.3:	AFRL measurement and Xpatch simulated results on 1.5MW turbine . (a) Measurment. (b) Predicion.	08
Figure 2.4:	Yaw angle effects at 16GHz, blades rotating in the plane coming out of page. (a) 90° yaw. (b) Backscattered spectrogram for 90° yaw. (c) 45° yaw. (d) Backscattered spectrogram for 45° yaw. (e) 0° yaw. (f) Backscattered spectrogram for 0° yaw.....	11
Figure 2.5:	ingle-arm wire model. (a) NEC-simulated backscattering. (b) NEC-simulated forward scattering. (c) Measured backscattering. (d) Measured forward scattering.	13
Figure 2.6:	Illustration of Doppler-inducing mechanisms seen in Fig. 2.5. (a) Backscattering mechanism (i). (b) Forward scattering mechanisms (ii) and (iii)..	14
Figure 2.7:	Single-arm wire excited by a plane wave. (a) Backscattering (b) Forward scattering.....	15
Figure 2.8:	Arm wire model. (a) NEC-simulated backscattering. (b) NEC-simulated forward scattering. (c) Measured backscattering. (d) Measured forward scattering.....	17
Figure 2.9:	Illustration of additional Doppler-inducing mechanisms seen in Fig. 2.4. (a) Backscattering mechanisms (i) and (ii). (b) Forward scattering mechanisms (iii) and (iv).....	18

Figure 2.10: Bergey turbine experimental setup..	19
Figure 2.11: Photo of the Bergey Windpower turbine. (b) Measured backscattering. (c) Measured forward scattering...	20
Figure 2.12: Blade shape effect based on a simple triangular blade model. (a) θ degrees before a blade flash occurs. (b) After 60 degrees of rotation. (c) Resulting irregular blade flashes as shown in black....	22
Figure 2.13: Spectrogram of a single rotating blade with a moving target behind. (a) Backscattering (b) Forward scattering.....	23
Figure 2.14: Illustration of additional Doppler-inducing mechanisms seen in Fig. 2.13. (a) Backscattering mechanisms (i) and (ii). (b) Forward scattering mechanisms (iii).....	24
Figure 2.15: Spectrogram of complete 3-arm model with a moving target behind. (a) Backscattering (b) Forward scattering.	25
Figure 2.16: Illustration of additional Doppler-inducing mechanisms seen in Fig. 2.15. (a) Backscattering mechanisms (i) and (ii). (b) Forward scattering mechanisms (iii).....	25
Figure 3.1: Gradual build up of the turbine using point scatterer model. (a) 3 point particles separated by 120 degrees phase angle (b) $M = 2$; linear spacing between scatterer = 7.5λ (c) $M = 3$; linear spacing between scatterer = 5λ (d) $M = 6$; linear spacing between scatterer = 2.5λ (e) $M = 15$; linear spacing between scatterer = λ (f) $M = 30$; linear spacing between scatterer = 0.5λ (g) $M = 60$; linear spacing between scatterer = 0.25λ (h) $M = 150$; linear spacing between scatterer = 0.1λ	30
Figure 3.2: Energy of the signal after basis subtraction for a single blade..	34

Figure 3.3: Basis parameterization applied on a two single blade of equal strength. (a) Original simulated data (b) spectrogram after 1 st residual subtraction (c) spectrogram after 2 nd residual subtraction (d) spectrogram after 3 rd residual subtraction... ..	35
Figure 3.4: Residual energy vs. residual iteration (10 iterations).....	36
Figure 3.5: Basis parameterization applied on a two single blade of un-equal strength; strength ratio 1:100. (a) Original simulated data (b) spectrogram after 1 st residual subtraction (c) spectrogram after 2 nd residual subtraction.	37
Figure 3.6: Residual energy vs. residual iteration (10 iterations).....	38
Figure 3.7: Ahilo results for a rectangular strip. (a) Strip geometry. (b) RCS at 0.1GHz. (c) spectrogram at 0.1GHz. (d) RCS at 1GHz. (e) spectrogram at 1 GHz.....	38
Figure 3.8: Ahilo results for a three rectangular strip. (a) RCS at 1GHz. (b) spectrogram at 1 GHz.....	41
Figure 3.9: Single blade simulation (a) Ahilo (b) point scatterer basis with $\lambda/10$ spacing between point scatterers.....	43
Figure 3.10: Basis parameterization applied on Ahilo data. (a) spectrogram after 1 st residual subtraction (b) spectrogram after 2 nd residual subtraction (c) spectrogram after 3 rd residual subtraction.	44
Figure 3.11: Residual energy vs. residual iteration on Ahilo data(10 iterations).	45

Chapter 1

Introduction

Wind energy is becoming an increasingly attractive option in today's world that is searching for alternative energy sources to reduce greenhouse gas emission. The world's wind energy supply has steadily increased in the past several years. With increasing interest in the wind energy arena, the number of wind farms worldwide can be expected to increase dramatically in the near future. This clean energy source can provide a solution to a potential future energy crisis and can possibly lead to cleaner air for current and future generations. With these benefits however, this new technology has also been observed to hinder performance of existing communications and radar systems.

The growth in the number of wind farms has raised concerns in the electromagnetic community due to the electromagnetic interference caused by wind turbines. Wind turbines have been known to interfere with television signals due to their large structure [1-4]. Also, their size and relative spacing may potentially cause deep electromagnetic shadows behind the wind farms. These effects may potentially hinder the ability of air traffic control and air defense radars in detecting objects flying inside the shadow region, and have been investigated in [5-15]. Moreover, the rotation of the turbine blades can produce Doppler frequencies of more than 2.5 kHz in the C-band and higher frequencies, which can coincide with the Doppler returns of aircrafts. This frequency overlap can make differentiating the Doppler from the turbine blades and an aircraft a very difficult task for air traffic control and air defense radars. Recently, wind farms have also caused concerns in the weather radar community [16-18].

The most ambitious and comprehensive investigation to date was carried out by the Air Force Research Lab (AFRL), in a study commissioned by the US Congress in 2006 [11-15]. The AFRL collected in-situ measurements of a single 1.5MW turbine on a wind farm in Fenner, NY. In their work, the AFRL successfully established the validity of the computational electromagnetics (CEM) code, X-patch, to model the returned signal from wind farms in order to avoid future field measurements. The most significant backscattering feature was found to be the blade flashes when the blades are oriented perpendicular to the radar line-of-sight. At all other positions of the blades, the blade tip was observed to trace a sinusoid in the spectrogram as it rotated. These results are quite similar to helicopter rotor blades, whose Doppler characteristics have been well studied previously [19-21]. In addition to these prominent features, other Doppler tracks were also observed in the data. They are potentially caused by higher-order multiple interactions, but were not fully explained. Furthermore, only the backscattered data of a single turbine was taken. The transmission blockage effect due to the wind turbine was not characterized in the study, which would have required a one-way forward scattering measurement with the transmitter and receiver being positioned on the two sides of the turbine.

The primary objectives of this thesis are to understand the Doppler characteristics of wind turbines in detail. Close examination of the Doppler characteristics of a single turbine is presented. The secondary objective is to devise a method to mitigate the backscattered Doppler clutter from the turbines in order to better observe the Doppler tracks from a moving target behind a wind farm. The algorithm developed for this purpose is in its early stage and has been tested only on simulated data.

Chapter 2 sets out to more closely examine the various Doppler features resulting from the scattering by a single turbine using a series of scaled model measurements. The

tested models include a 1:160 scaled model turbine, a 3-arm wire model, and a small wind turbine from Bergey Windpower with 2' blades. The results of the 1:160 scaled model turbine are discussed first. It is shown that our scaled model measurements captured the essential Doppler features observed in [11-15]. Next, multiple scattering effects observed in the wire model turbine and the forward Doppler arising due to multiple scattering are described. We also report on the near field effects resulting from close spacing between the radar and the model turbines. The Doppler features resulting due to the unique shape of the Bergey wind turbine blades are discussed. Finally, the effects of the presence of a moving target behind a turbine on the resulting Doppler features are analyzed.

Chapter 3 discusses a technique to mitigate the strength of the radar cross section (RCS) signal received from the wind turbines. A moving target behind a wind farm can be very hard to observe due to its weaker signal relative to wind turbines. We propose a set of basis function that closely match the RCS of the wind turbine and perform an iterative subtraction of the projection of our basis function onto the received signal. This iterative subtraction method can reduce the intensity of the turbine return, thus making possible the tracking of moving targets behind the wind farm. This algorithm is applied to the backscattered signal generated from a large size wind turbine obtained using Ahilo, which is a newly developed software that uses high-frequency ray tracing to calculate the RCS from the turbine.

Chapter 2

Multiple Scattering Studies on Scaled Turbine Models

This chapter presents the close examination of the Doppler features in wind turbines through a series of scaled model measurements. Both backscattered and forward scattered data are measured at Ku-band from various wind turbine models undergoing rotation. The tested models include a 1:160 scale model turbine, a 3-arm wire model, and a small wind turbine from Bergey Windpower with 2' blades. Detailed accounts of the physics behind the observed phenomena including multiple scattering, near field effects, and blade shape effects are presented. We first report on the results of the 1:160 scaled model turbine and show that our scaled model measurements capture the gross Doppler features observed in [11-15]. We then describe the multiple scattering and near field effects observed in the wire model turbine. The experimental findings are corroborated by simulations performed using the Numerical Electromagnetics Code (NEC). For forward scattering, it is shown that Doppler features can only arise due to multiple scattering. Next, the Doppler features in the Bergey Windpower turbine are reported. Its blade shape effect is discussed. Finally, analysis of Doppler features of the wire model with a target moving behind the model is presented.

2.1 Methodology

A vector network analyzer (*Agilent N5230A*) was used to collect measurement data in continuous wave (CW) mode at 14 GHz. For the 3-arm wire model and the Bergey Windpower turbine, the data was collected for 65.5 seconds, which corresponds

to one rotational period of our turn-table, while the sampling rate was set at 22Hz. The data were sampled for a total of 1441 points. The 1:160 scaled model turbine is driven by a motor with a period of 1.67 seconds. Therefore, data were collected for 5 seconds at a sampling rate of 160 Hz which corresponds to 800 total sampled points. The intermediate frequency (IF) bandwidth was set at 200 Hz for the 1:160 model and 30 Hz for the other two models. The instrument dictates that the IF bandwidth must be greater than the pulse repetition frequency. However, higher IF bandwidth results in higher noise level in the collected data. Therefore it was set at the minimum values allowed. Two horn antennas, separated by 4m, were set facing each other and the turbine under test was placed in between, 2 m from each horn. Both S11 and S21 parameters were measured for each turbine model. We also performed background subtraction for each S-parameter to reduce the effects of reflection within the horn and direct coupling between the horns, which give rise to a very strong zero-Doppler component. The complex scattering data for each parameter was processed using the short-time Fourier transform (STFT).

Unlike with the conventional Fourier transform, the STFT is a good tool to capture the time-varying Doppler characteristics of a signal [28]. Eq. 2.1 gives the mathematical representation of the STFT:

$$STFT\{x(t)\} = X(\tau, \omega) = \int x(t)w(t - \tau)e^{-j\omega t} dt \quad (\text{eq. 2.1})$$

The short-time Fourier transform takes the Fourier transform of the original time domain signal, $x(t)$, multiplied with a sliding finite window function, $w(t)$.

For the discrete time case, the continuous independent variables in (eq. 2.1) are replaced with discrete indexes as evident in (eq. 2.2):

$$STFT\{x[n]\} = X(m, \omega) = \sum x[n]w[n - m] e^{-j\omega n} \quad (\text{eq. 2.2})$$

The discrete form of the STFT takes Fourier transform of a short-time segment of a signal and assigns the magnitude of the result to the time value corresponding to the center of the window function. This procedure is shown in Fig. 2.1,

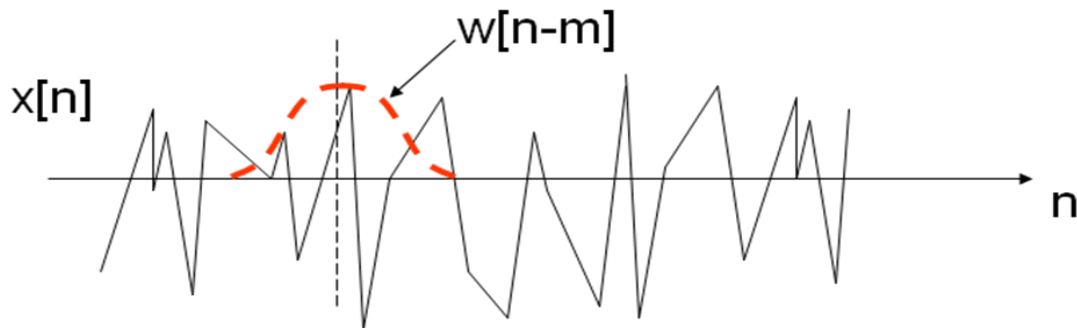


Fig. 2.1. Graphical illustration of the discrete short time Fourier transform

where $x[n]$ is the discretized signal. The window function shown in the red dashed curve determines the amount of signal being sampled and the resulting Fourier transform of the segment is assigned to the time value at the black dashed line. The window function is next slid to the right and this process is repeated. Adjacent windows may overlap in the sliding. This process is iterated until the STFT of the complete signal is obtained. The magnitude of the resulting function is referred to as the spectrogram. The spectrogram is plotted on a 2-D time-frequency plot to obtain the Doppler characteristics of the signal as a function of time. A large time window leads to worse time resolution but better resolution along the frequency dimension. This relationship between time and frequency is swapped for the case of small time window. The size of the time window should be roughly comparable to the periodicity of the signal in order to capture the instantaneous

time-varying frequency characteristics of the signal. Under this consideration, a time window of 0.4 second is used to process the 1:160 scaled model turbines and a 6-second window was used for the other two models.

2.2 DOPPLER FEATURE ANALYSIS

2.2.1 The 1:160 Scaled Model

Fig. 2.2(a) shows the 1:160 scaled model turbine (Model Power No. 1583). Each blade is 12 cm in length. The turbine was covered with aluminum tape during the measurement to enhance the strength of the received signal. Fig.2.2(b) shows the resulting spectrogram from the measured backscattered data at 90° yaw angle (edge-on incidence). Clearly seen are the blade flashes that occur at every 60° turn of the turbine. The flashes alternate between positive Doppler (as a blade moves toward the radar) and negative Doppler (when the next blade recedes away from the radar). In addition, a set of weaker, sinusoidal Doppler tracks can be observed. They are due to scattering from the blade tips and are labeled as “tip halo” in the figure. As the yaw angle is changed from 90° to 0° (nose-on), the amount of Doppler shift decreases, as the radial velocity of the blades with respect to the radar is decreased. It should be pointed out that, since the model measurement was conducted at 14GHz for the 1:160 scaled model, the results here should correspond to a real turbine at only $14\text{GHz}/160=0.0875\text{GHz}$. Nevertheless, when compared to the data from a full-scale 1.5 MW turbine collected between 1 to 10GHz by AFRL in [11-15], the same key features are observed. A sample of the measured and simulated data by AFRL is shown in Fig. 2.3. The blade flashes and tip halos seen in the full scale turbine results are also present in the scaled model measurements.

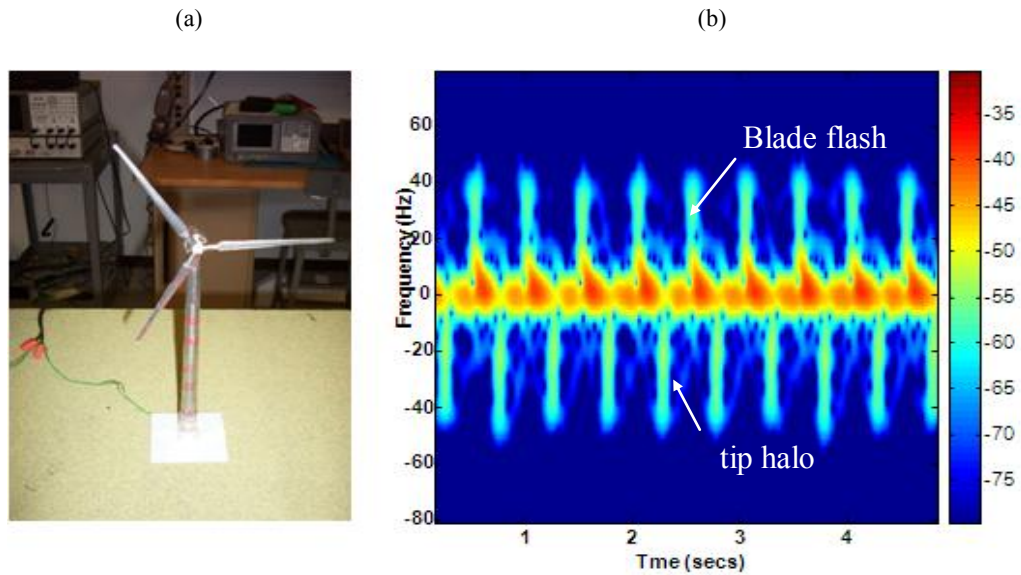


Fig. 2.2. 1:160 scaled model turbine measurements. (a) Photo of the model turbine. (b) Backscattered spectrogram after STFT processing.

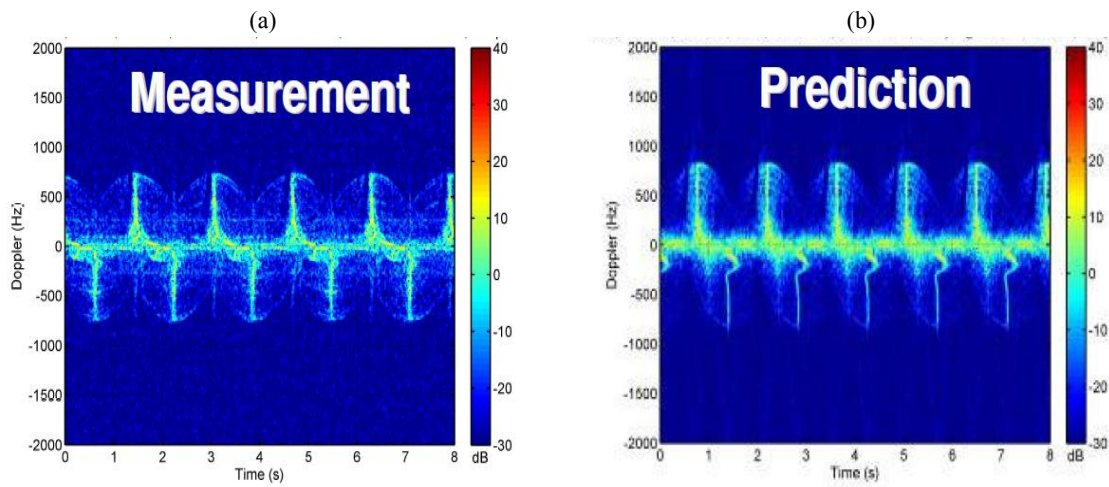


Fig. 2.3. AFRL measurement and Xpatch simulated results on a 1.5MW turbine. (a) Measurement. (b) Prediction.

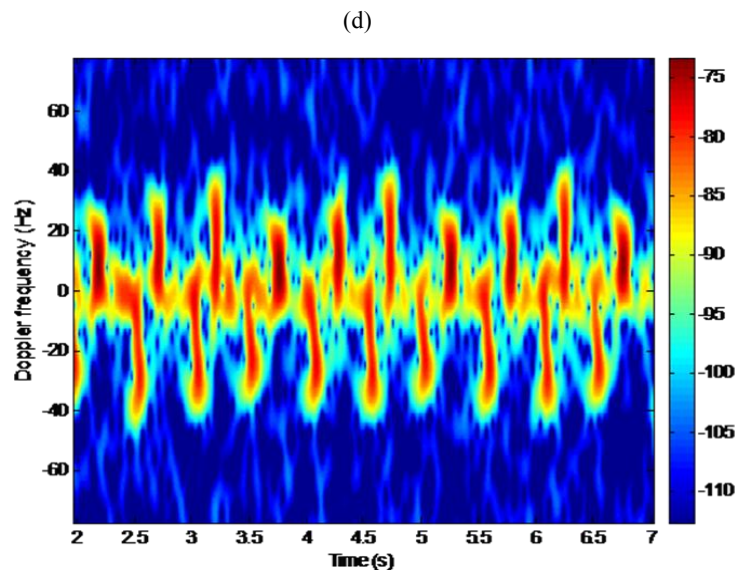
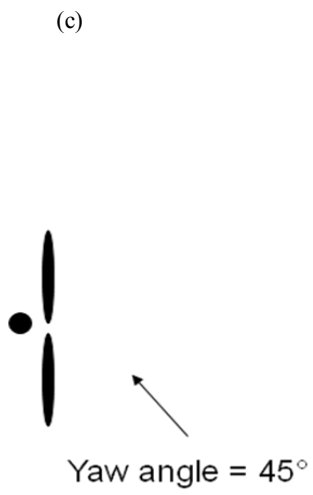
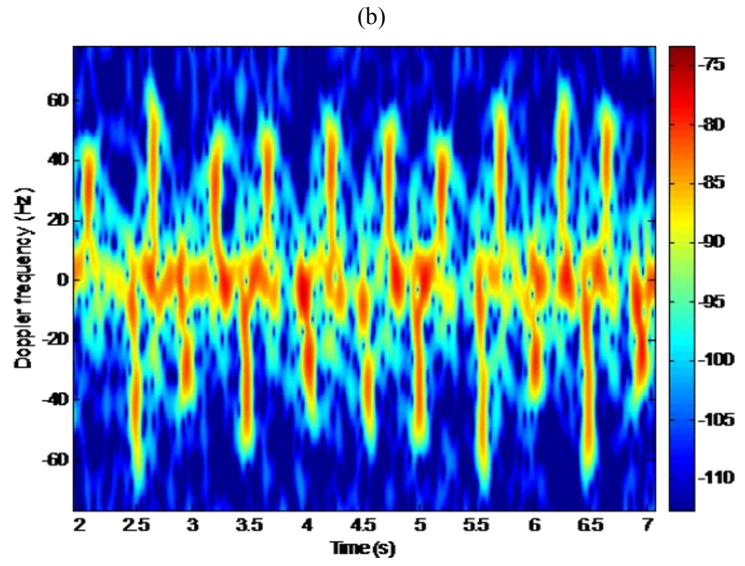
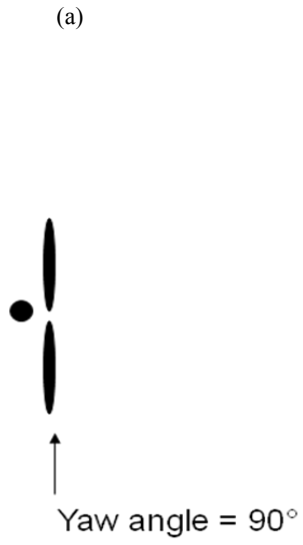
Fig. 2.4 illustrates the effects of the yaw angle on the resulting Doppler features. The backscattered data is collected at 16 GHz. In Figs. 2.4 (a), (c), and (e) the blades are assumed to be rotating towards out of the page and the arrow represents the direction of incident ray on the turbine blades. In the corresponding spectrogram, the maximum Doppler can be seen to decrease with decreasing yaw angle. This effect is the result of the decrease in the radial velocity of the blades towards the radar. Generally, the backscattered maximum Doppler from blades is given by

$$f = 2v_r/\lambda \quad (\text{eq. 2.3})$$

where v_r is the radial velocity of the blades towards the radar and λ is the incident wave length. The velocity v_r can be written as

$$v_r = v * \sin(\theta) \quad (\text{eq. 2.4})$$

where v is the maximum rotational velocity of the blades and θ is the yaw angle. This equation shows that decreasing yaw angle causes a decrease in the maximum resulting Doppler. Figs. 2.4 (b), (d), and (f) show this transition for 90, 45, and 0 degree yaw angle.



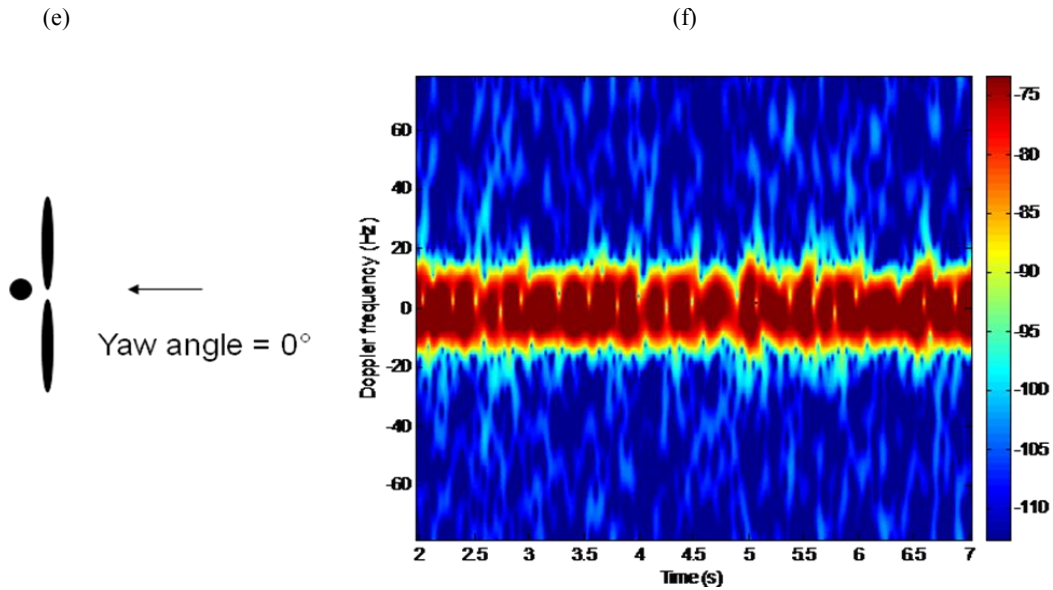


Fig. 2.4. Yaw angle effects at 16GHz, blades rotating in the plane coming out of page. (a) 90° yaw. (b) Backscattered spectrogram for 90° yaw. (c) 45° yaw. (d) Backscattered spectrogram for 45° yaw. (e) 0° yaw. (f) Backscattered spectrogram for 0° yaw.

2.2.2 3-Arm Wire Model

Next we constructed a 3-arm wire model that is 5 times longer than the 1:160 scaled model and investigate its Doppler scattering features. The electrical length of the blade at 14 GHz is 30λ . Longer blades more closely model the size of real turbines at common frequencies. It also leads to better resolution of the scattering phenomenology in the resulting spectrogram. While the structure chosen is quite simplistic, its scattering can be examined in closer detail by building up the structure one wire arm at a time. Furthermore, the measurement results can be verified through simulations using NEC.

The simulations are performed with the same settings as described for the measurements and are processed in the same manner as well.

We start by analyzing the scattered data from a single blade. Figs. 2.5(a) and 2.5(b) show the spectrograms from the backscattered and forward scattered data simulated using NEC. Figs. 2.5(c) and 2.5(d) are the corresponding measured results. The simulation and measurement results are plotted over the same dynamic range, although the absolute level of the measurements was not calibrated. Several new features are noted in addition to the blade flashes and tip halos discussed previously. First, we see from the backscattered spectrogram in Fig. 2.5(a) an additional sinusoid track that is in phase with the tip halo (labeled as (i)). This additional track is due to a traveling wave along the wire from the tip to the hub, and vice versa, as illustrated in Fig. 2.6(a). The blade in Fig. 2.6(a) rotates clock-wise and the bottom end of the blade is the center of rotation. Therefore, the two traveling waves along the wire in Fig. 2.6(a) experience a path length change versus time that is only half as large as the direct scattering due to the top tip. Hence this interaction results in a Doppler track with a maximum Doppler shift equaling half that of the tip halo. As a note, the slight overshoot in the flash seen in Fig. 2.5 (c) is due to the slight wobble in the rotating wire during measurement.

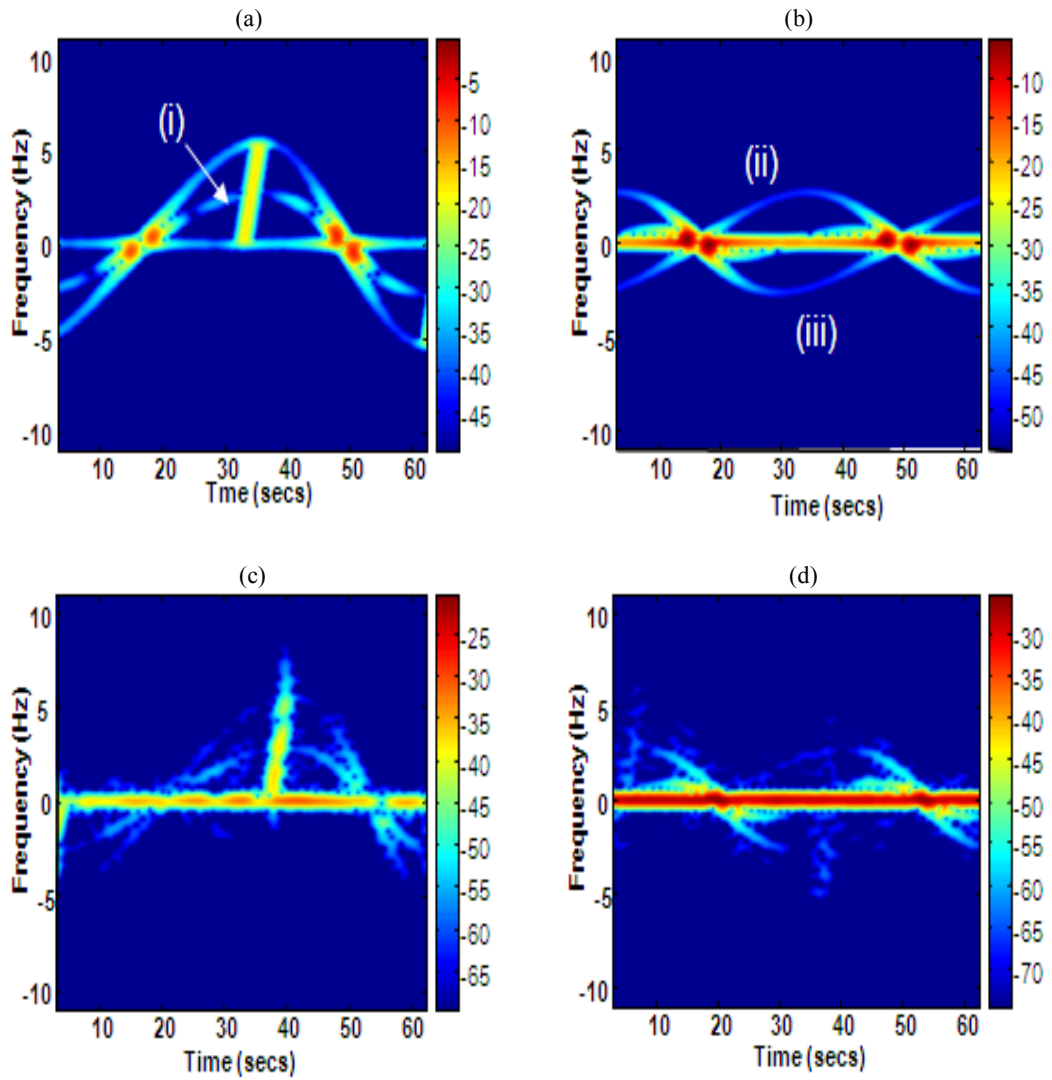


Fig. 2.5. Single-arm wire model. (a) NEC-simulated backscattering. (b) NEC-simulated forward scattering. (c) Measured backscattering. (d) Measured forward scattering.

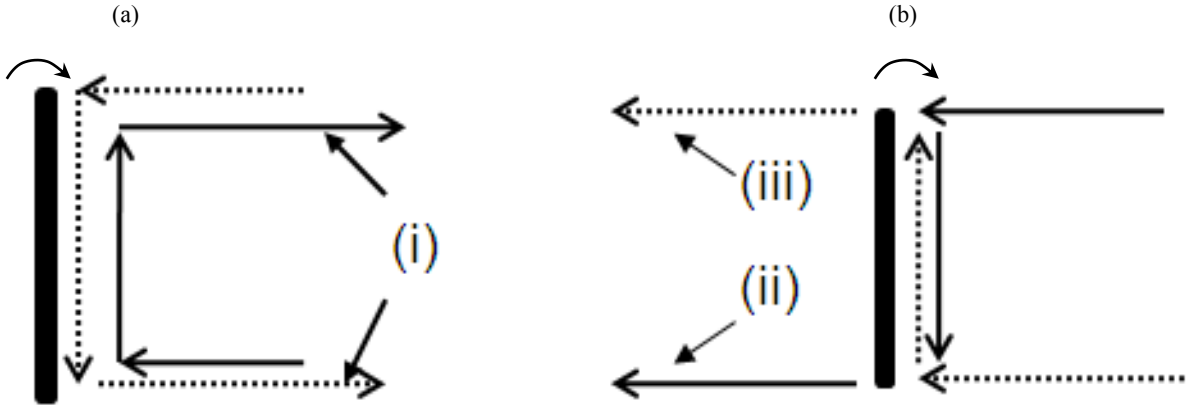


Fig. 2.6. Illustration of Doppler-inducing mechanisms seen in Fig. 2.5. (a) Backscattering mechanism (i). (b) Forward scattering mechanisms (ii) and (iii).

For the forward scattering case, the sinusoidal tracks labeled (ii) and (iii) in Fig. 2.5(b) are the results of the multiple interactions illustrated in Fig. 2.6(b). In the interaction labeled as (ii), the wave experiences a decrease in path length as a function of time since the top tip moves toward the transmitter. However, in traveling down to the base of the wire and toward the receiver, no additional path length change is encountered. Therefore, this interaction gives rise to a sinusoid that has a positive Doppler shift with maximum equal to half that from the tip halo backscattering. The case labeled as (iii) Fig. 2.6(b) gives rise to a negative sinusoidal peak since the wave experiences an increase in path length as a function of time as it travels from the top tip to the receiver. We note that while the Doppler features in backscattering arise from both single and multiple scattering, forward Doppler can only result from multiple scattering interactions. Any single scattering phenomenon will result in only zero Doppler contribution in the forward direction.

Lastly, we observe that the blade flashes in the backscattering data in Figs. 2.5(a) and 2.5(c) are tilted. In this case, the NEC simulation is carried out with a near-field

source and receiver. This step is taken in order to emulate the measurement setup. As a result, the specular reflection occurs at different times for different points on the blade, which leads to the slanted shape of the flashes. Near field effect is also the reason behind the sinusoidal Doppler tracks in the forward scattering (features (ii) and (iii) in Fig. 2.5(b)) not being exactly 180° out of phase. Indeed, for a plane wave excitation the blade flashes become straightened, Fig. 2.7(a), and the forward Doppler tracks are perfect sinusoids with 180° phase difference as illustrated in Fig. 2.7(b).

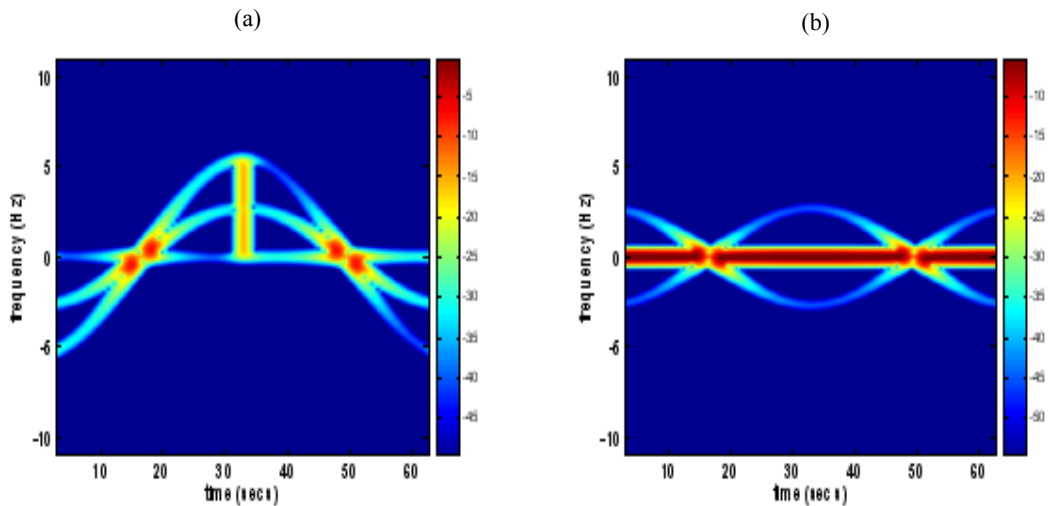
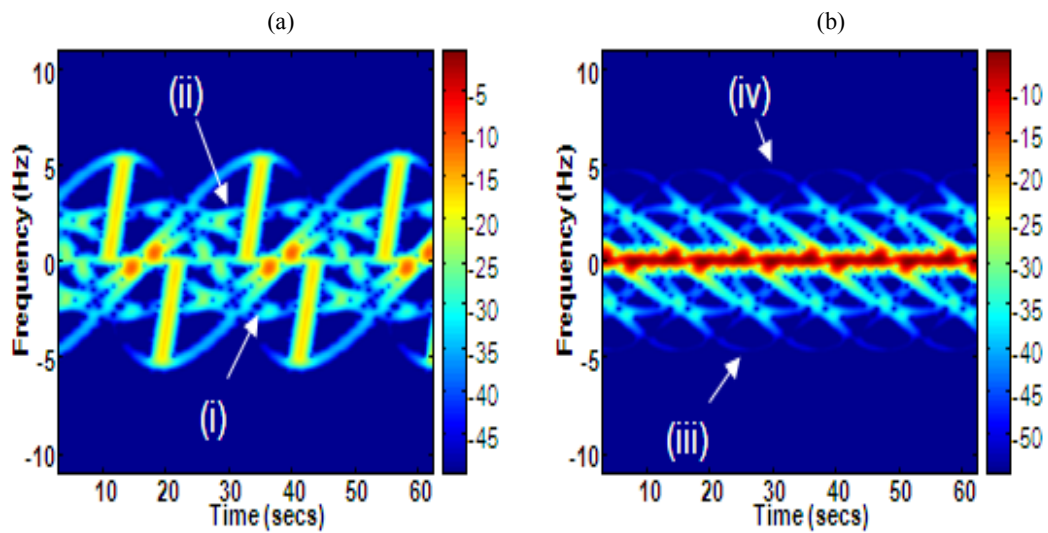


Fig. 2.7. Single-arm wire excited by a plane wave. (a) Backscattering (b) Forward scattering.

The spectrograms of the backscattered and forward scattered data for the complete 3-arm wire model are shown in Fig. 2.8. Figs. 2.8(a) and 2.8(b) show the spectrograms from respectively the backscattered and forward scattered data simulated using NEC. Fig. 2.8(a) shows that in addition to the intra-blade backscattering interaction seen for a single blade, we also observe an additional sinusoidal track, whose maximum

Doppler value is labeled (i) in Fig. 2.8(a). Fig. 2.9(a) shows the turbine position at which this track peaks and the mechanism giving rise to it is illustrated. Fig. 2.9(a) also explains why this track peaks on the opposite side of the blade flash. The two blades involved in the interaction are at 30° to the horizontal, hence the maximum Doppler value of v/λ . The mechanism behind the track labeled (ii) in Fig. 2.8(a) is explained in Fig. 2.9(a) and has already been discussed.



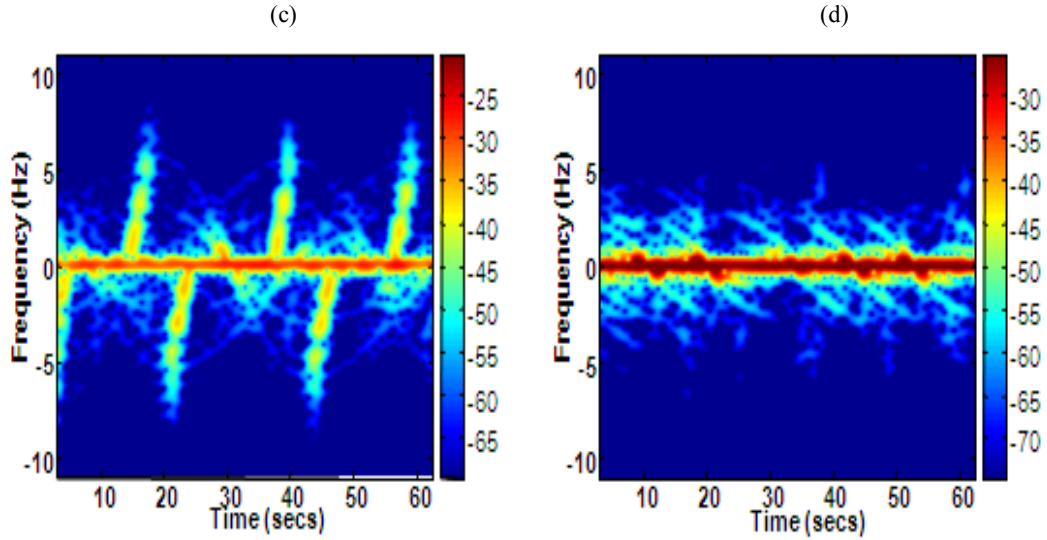


Fig. 2.8. 3-Arm wire model. (a) NEC-simulated backscattering. (b) NEC-simulated forward scattering. (c) Measured backscattering. (d) Measured forward scattering.

In the forward scattering spectrogram in Fig. 2.8(b), we also see inter-blade interactions that result in a maximum Doppler shift of $\sqrt{3}v/\lambda$ along with the tip-to-base interaction described earlier, which gave rise to a maximum Doppler of only v/λ . In Fig. 2.8(b), the Doppler tracks labeled (iii) and (iv) are illustrated in Fig. 2.9(b). We notice that while tip-to-base interaction tracks peak when the blade is perpendicular to the incident wave, tip-base-tip interaction peaks when the blades are 60° to the horizontal. Because of the three bladed symmetry of the structure, the tracks for the backscattered data change signs every 60° while forward scattered Doppler tracks are repeated after every 60° rotation.

Figs. 2.8(c) and 2.8(d) are the corresponding measured results. They show fair agreement with the simulations. While we clearly see the tip-to-base interaction in Fig.

2.8(a), the weak tip-base-tip interaction seen in Fig. 2.8(b) does not show up very clearly. The reason for the absence of the tracks is the difficulty in replicating the exact simulation set up and due to insufficient signal-to-noise in the measurement. We also examined potential turbine-ground interactions by placing a large metal plate next to the wire model. However, such interaction was too weak to be observed.

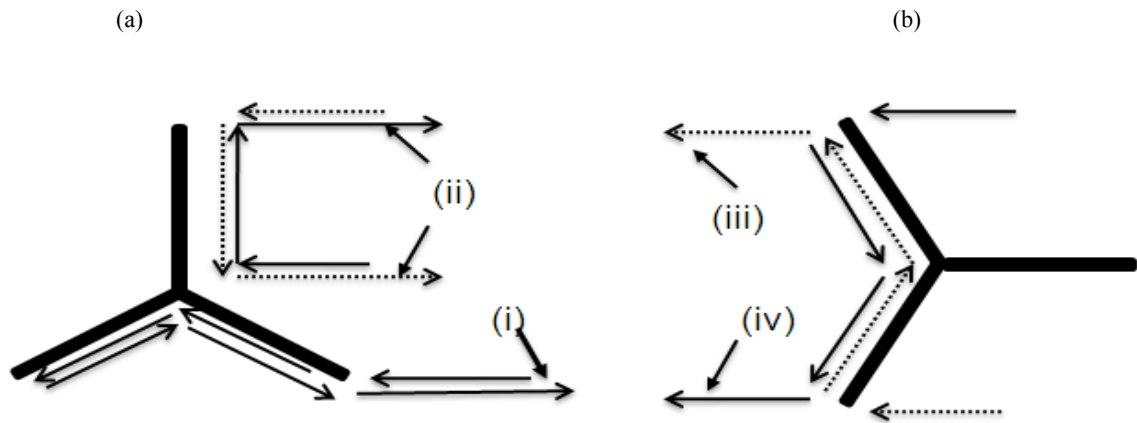


Fig. 2.9. Illustration of additional Doppler-inducing mechanisms seen in Fig. 2.4. (a) Backscattering mechanisms (i) and (ii). (b) Forward scattering mechanisms (iii) and (iv).

2.2.3 Bergey Windpower Turbine

Following the findings on the 3-arm wire model, we measured a small commercial wind turbine that is the same size as the wire model. The blades of the turbine are manufactured from carbon fiber material. The experimental setup is shown in Fig. 2.10 while the turbine is shown in Fig. 2.11(a). Interestingly, covering the blades by aluminum tape did not significantly increase the measured strength of the scattering. The backscattering, shown in Fig. 2.11(b), shows two interesting features that are distinct

from the previous two models, namely, curved flash shape and uneven spacing between the flashes. They are attributable to the unique shape of the turbine blades as can be seen in Fig. 2.11(a). The forward scattering spectrogram is shown in Fig. 2.11(c). Although forward Doppler can be observed, it does not show any clear tracks.

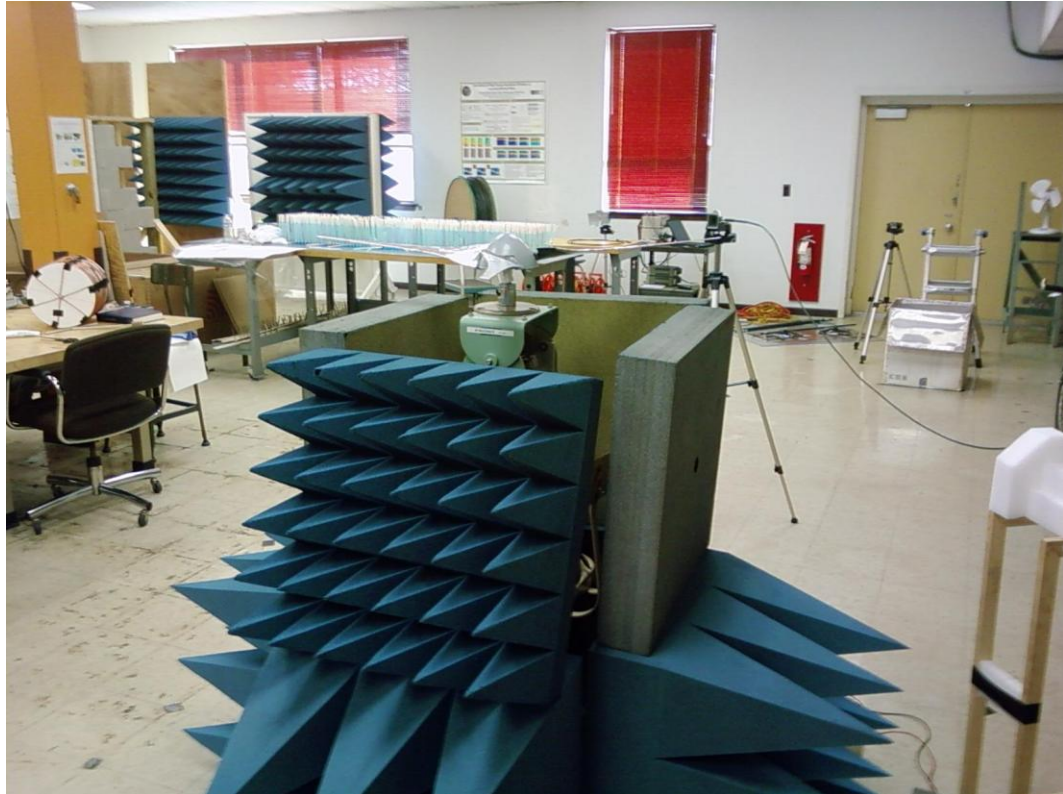


Fig. 2.10. Bergey turbine experimental setup.

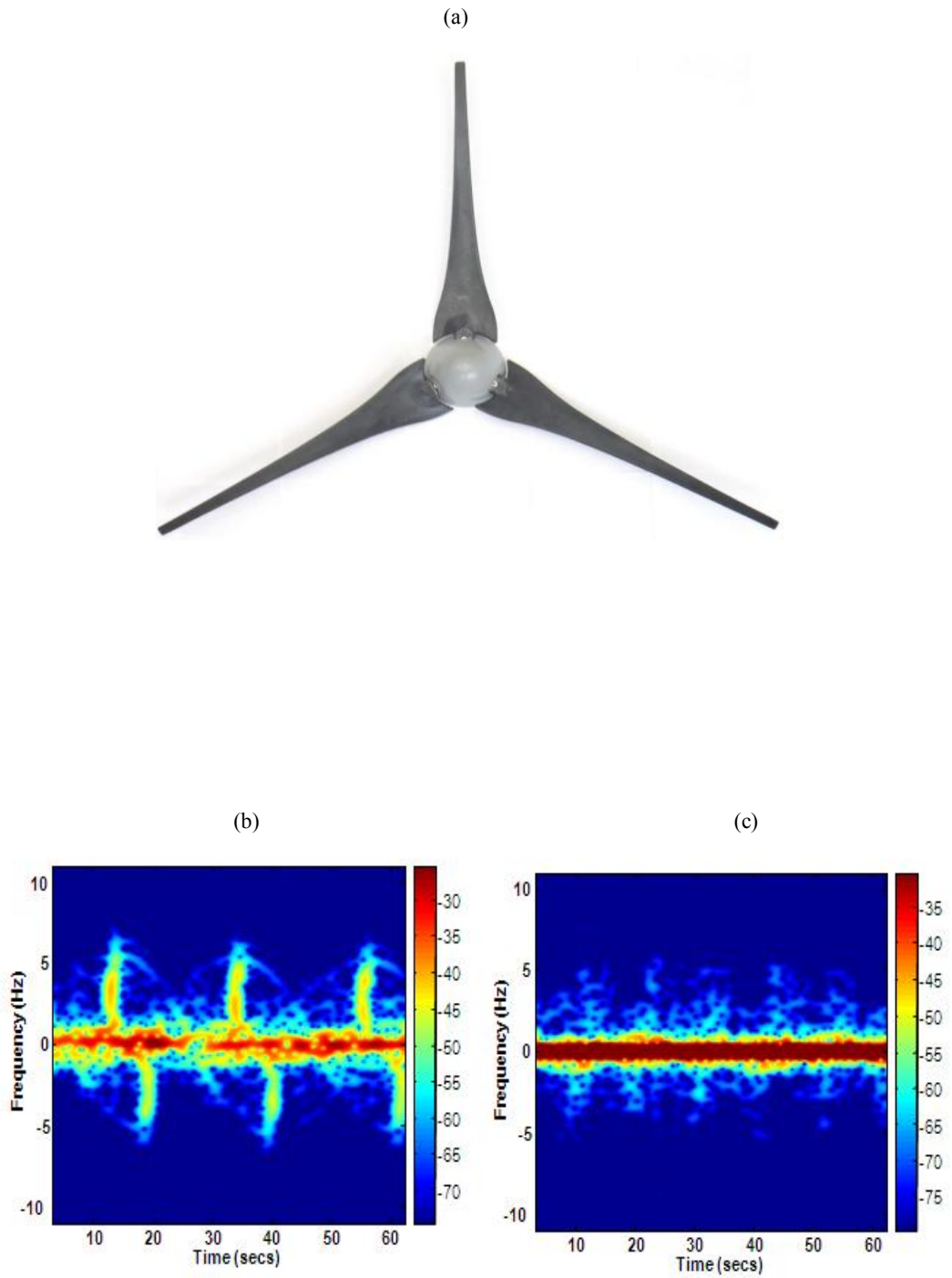
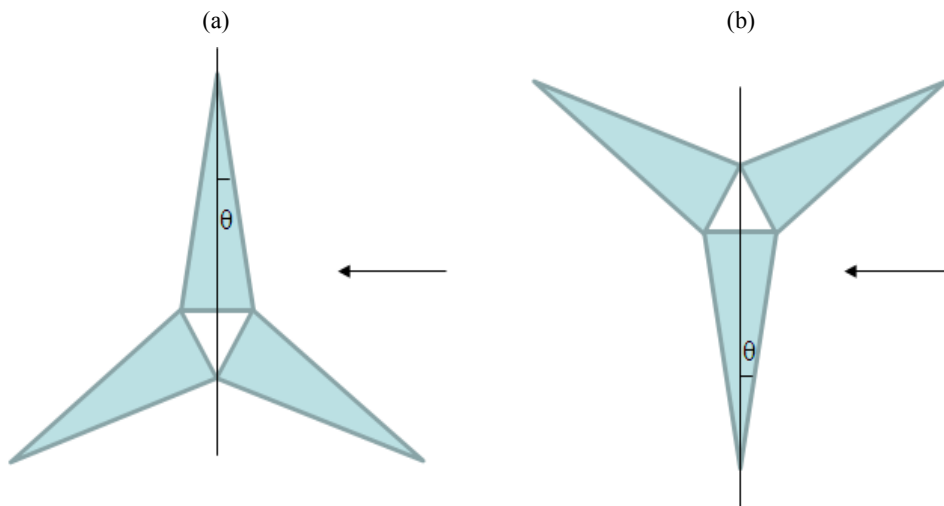


Fig. 2.11. (a) Photo of the Bergey Windpower turbine. (b) Measured backscattering. (c) Measured forward scattering.

To understand the irregular flashing behavior in the backscattering, we consider a simpler model comprising triangular-shaped turbine blades shown in Fig. 2.12. In Fig. 2.12, the blades are assumed to rotate clockwise. For this simple model, the edge of the triangular turbine blade does not become perpendicular to the radar in the orientation shown in Fig. 2.12(a), but at θ degrees later (where 2θ is the inscribed angle of the blade). This results in a delayed flash, as marked by the first black line in Fig. 2.12(c). The next flash also does not occur in the position shown in Fig. 2.12(b) but at θ degrees earlier. Therefore the interval between two flashes is decreased by 2θ . On the other hand, the next interval is lengthened by 2θ . Fig. 2.12(c) illustrates this effect. The blue flashes shown are normal equally spaced flashes that are 60° apart. The black flashes shown are from a triangular shaped blade occurring in the angular intervals described above. Note that even for a small θ value of 15° , the adjacent flash spacing becomes 30° - 90° instead of 60° - 60° , i.e., to an interval ratio of 1:3 instead of equally spaced. This can explain why the blade flashes in the real turbine are so unevenly spaced.



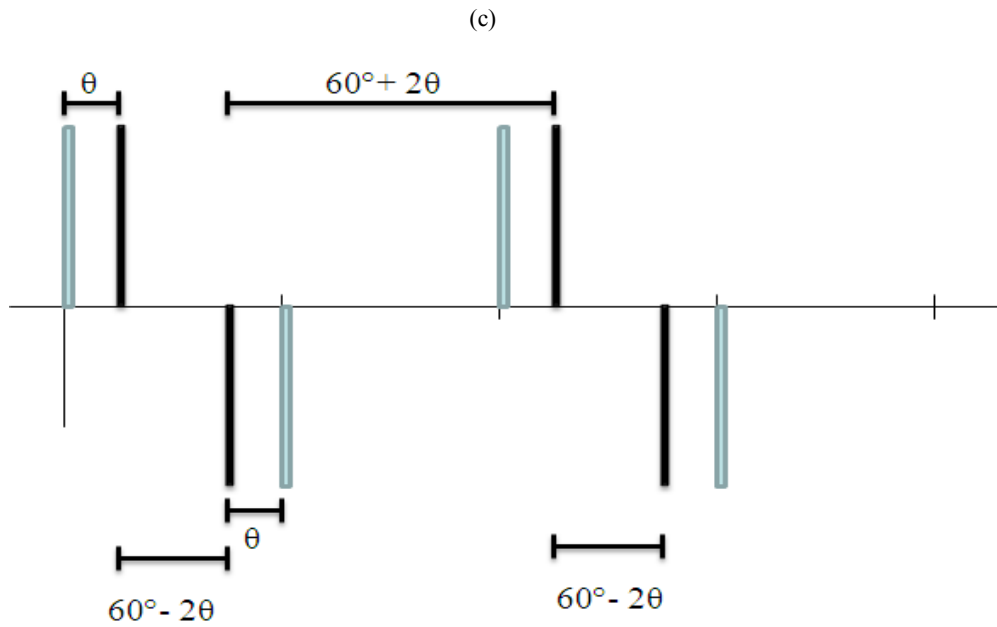


Fig. 2.12. Blade shape effect based on a simple triangular blade model. (a) θ degrees before a blade flash occurs. (b) After 60 degrees of rotation. (c) Resulting irregular blade flashes as shown in black.

2.3 Moving Target Behind the 3-Arm Wire Model

The previous sections provides with valuable insights into the Doppler features from the turbine models only. This section presents the effects on the resulting Doppler of a constant velocity moving target behind the turbine. The target starts at about 200λ from the center of rotation of the wire and moves to within 100λ of the center. It travels a physical distance of 2 m in one full rotation of the turbine. Fig. 2.13 shows the

resulting Doppler due to the presence of a moving target in addition to a single rotating blade.

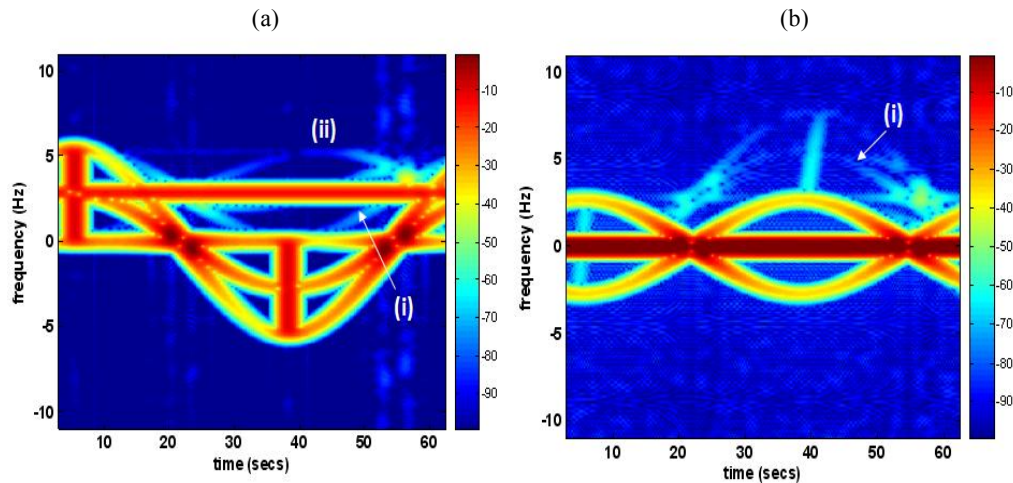


Fig. 2.13. Spectrogram of a single rotating blade with a moving target behind. (a) Backscattering (b) Forward scattering.

The backscattering, Fig. 2.13 (a), contains the blade flash, the tip halo and the tip to hub return discussed previously. Moreover, it also contains a constant Doppler track at 3 Hz and two very weak slightly asymmetric out of phase sinusoids centered about the constant Doppler track. The constant Doppler is the result of the motion of the moving target while the sinusoids are the results of the multiple interactions between the blade and the target. The mechanism giving rise to this interaction is shown in Fig. 2.14(a). As shown in Fig. 2.14(a), the sinusoids are the result of the rays that return from the target, travel along the wire, and return to the receiver. The path that the waves encounter after returning from the target is the exact path that forward Doppler causing waves encounter for the case of a single rotating blade. This explains the sinusoidal shape of tracks. The shift by 3 Hz is due to the earlier interaction between the wave and the target behind the

wire. In the forward scattering, the multiple interaction between the target and wire result in tracks resembling backscattering from a single blade as evident in Fig. 2.14 (b). Also, the sinusoids in 2.13(a) are slightly asymmetric and the flashes in Fig. 2.13 (b) are tilted. These two features are the result of the target's presence within the near field of the blade.

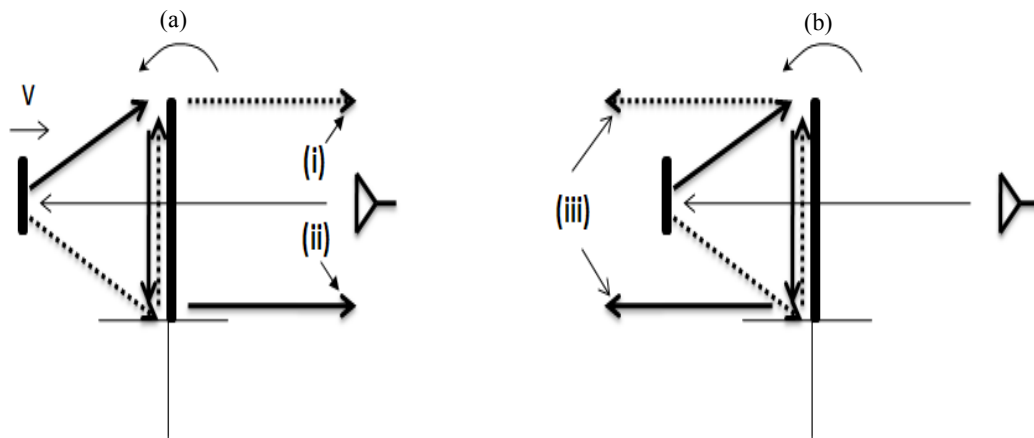


Fig. 2.14. Illustration of additional Doppler-inducing mechanisms seen in Fig. 2.13. (a) Backscattering mechanisms (i) and (ii). (b) Forward scattering mechanisms (iii).

Fig. 2.15 shows the Doppler tracks between a mover and full 3-arm wire model. The backscattering shows the forwards scattering resembling tracks due to the mover-turbine interaction. The interaction labeled (i) is the result of the wave that travels back from the target and subsequently encounters the inter-blade multipath interaction shown in Fig. 2.16(a). The interaction labeled (ii) in 2.16(b) is not clearly seen in Fig. 2.15(a) because these Doppler tracks coincide with the much stronger and closely pack Doppler features of the turbine blades. Finally, the mover-turbine forward interaction leads to Doppler track that resemble backscattering. The mechanism labeled (iii) in Fig. 2.16(b) explains the presence of the negative flash in the spectrogram. The positive flashes are

not clearly seen for the same reason that interaction (ii) is not seen in Fig. 2.15(a). Fig. 2.15 demonstrates that the Doppler arising from a radar signal propagating through a wind farm will comprise of both forward and backscattering tracks.

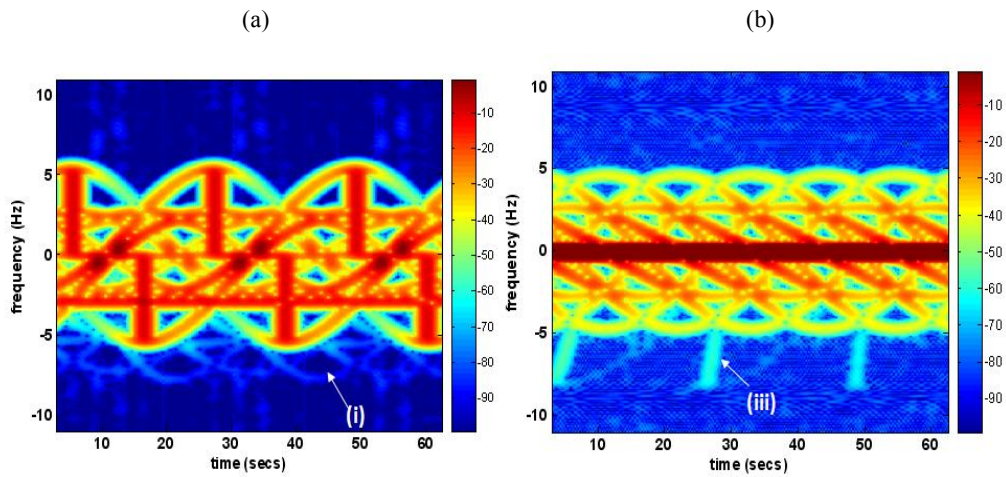


Fig. 2.15. Spectrogram of complete 3-arm model with a moving target behind. (a) Backscattering (b) Forward scattering.

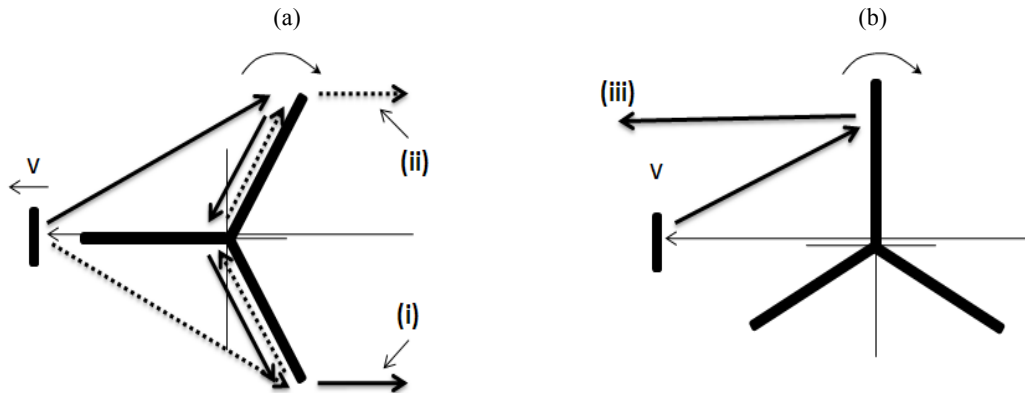


Fig. 2.16. Illustration of additional Doppler-inducing mechanisms seen in Fig. 2.15. (a) Backscattering mechanisms (i) and (ii). (b) Forward scattering mechanisms (iii).

Chapter 3

A Signal Filtering Technique to Remove Doppler Clutters Caused by Wind Turbines

In Chapter 2, the Doppler clutter produced by turbines was analyzed in detail. With the physics of the Doppler clutter well understood, this chapter provides a preliminary investigation into the filtering of the Doppler clutter caused by wind turbines so that real moving targets can be more easily detected. Previously, a filtering technique has been investigated by utilizing a multiquadratic interpolation technique to filter out the turbine clutter [22]. Other possible mitigation measures including signal processing, active signal cancellation, and RCS reduction using stealth material have been discussed by [23-26]. Also, removing helicopter rotor effects have been investigated by Wang et al. to filter out time-varying Doppler signals in [27]. In this chapter, a simple physical model of the turbine scattering is used to filter out the Doppler signal. The simulated RCS from the physical model can be used as the basis function to represent the signal from the turbine blade. Proper strength coefficient for the basis function can be found by projecting the basis function onto the turbine return signal using a process analogous to finding Fourier series coefficients. The resulting function can be subtracted from the turbine signal to reduce in strength or eliminate the turbine tracks in the spectrogram.

In this chapter, first, the scattering from blades is modeled using point scatterer similar to the models presented in [21] and [28]. It will be shown that, barring the weak higher order interactions, its time-frequency characteristics very closely resemble that of an actual turbine. Next, the method to obtain the strength coefficients for the basis

function is described. Following on, an iterative subtraction is performed on the return signal using the basis function. This method is applied to the point scatterer and Ahilo simulated data to demonstrate its effectiveness in reducing the strength of the turbine return signal.

3.1 Point Scatterer Model

Mathematically, the signal from a single rotating point scatterer about a fixed center can be written as:

$$\Phi(t) = e^{-2jkR\sin(\omega t + \theta)} \quad (\text{eq. 3.1})$$

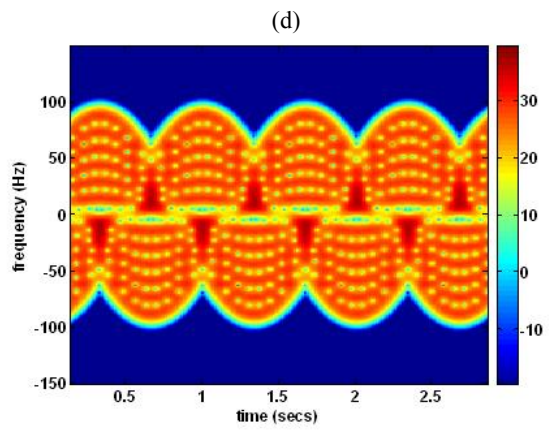
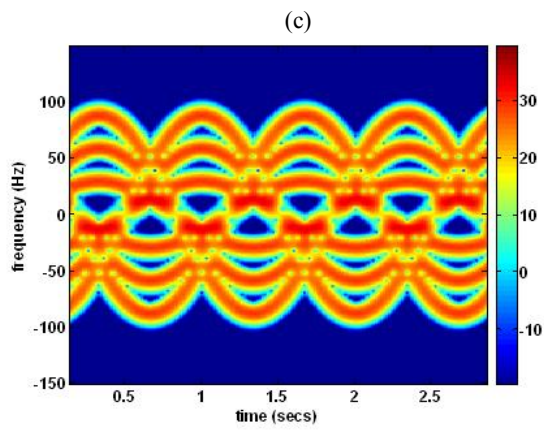
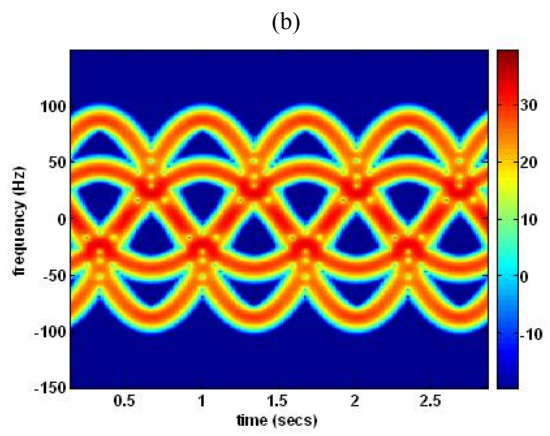
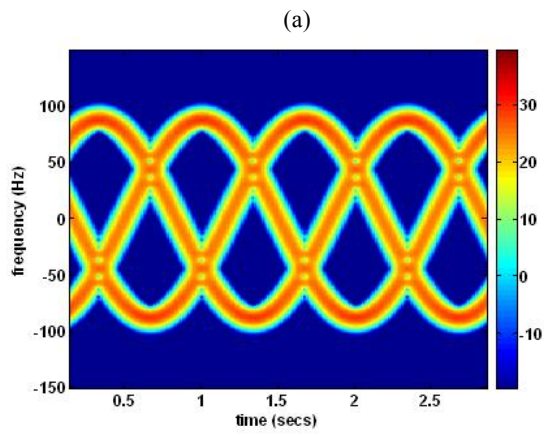
where k is the propagation constant, R is the distance of the point particle from the center of rotation, ω is the angular velocity, and θ is the phase angle. It will be shown that as the spacing between the point particles is decreased, the backscattered signal more closely resembles the signal from a single turbine blade's rotation. The close spacing of the point particles can be modeled by eq. 3.2

$$\Phi(t) = \sum_{m=1}^M e^{-2jkR_m\sin(\omega t + \theta)} \quad (\text{eq. 3.2})$$

Equation 3.2 can model the signal from a signal blade, where the index m controls the linear spacing of point scatterers. Eq. 3.2 can be modified to account for the signal from an arbitrary number of blades by adding an additional index which controls the angular spacing between the blades as shown in eq. 3.3

$$\Phi(t) = \sum_{m=1}^M \sum_{n=1}^N e^{-2jkR_m \sin(\omega t + \theta_n)} \quad (\text{eq. 3.3})$$

Fig. 3.1 slowly builds up a full turbine using eq. 3.3. In Fig. 3.1(a), M is set to 1 while N is set to 3 and each scatterer is separated by the other by a 120 degrees phase angle. More point scatterers are gradually added, in other words M is increased, which decreases the linear spacing between the point particles. When the linear spacing between the scatterers becomes $\lambda/2$, Fig. 3.1 (f), we observe the flashes and tip halos seen in the turbine results. Also, the Doppler features of the results are convergent thereafter as M is increased in order to decrease the linear space between adjacent point particles, figs 3.1(e) and (f).



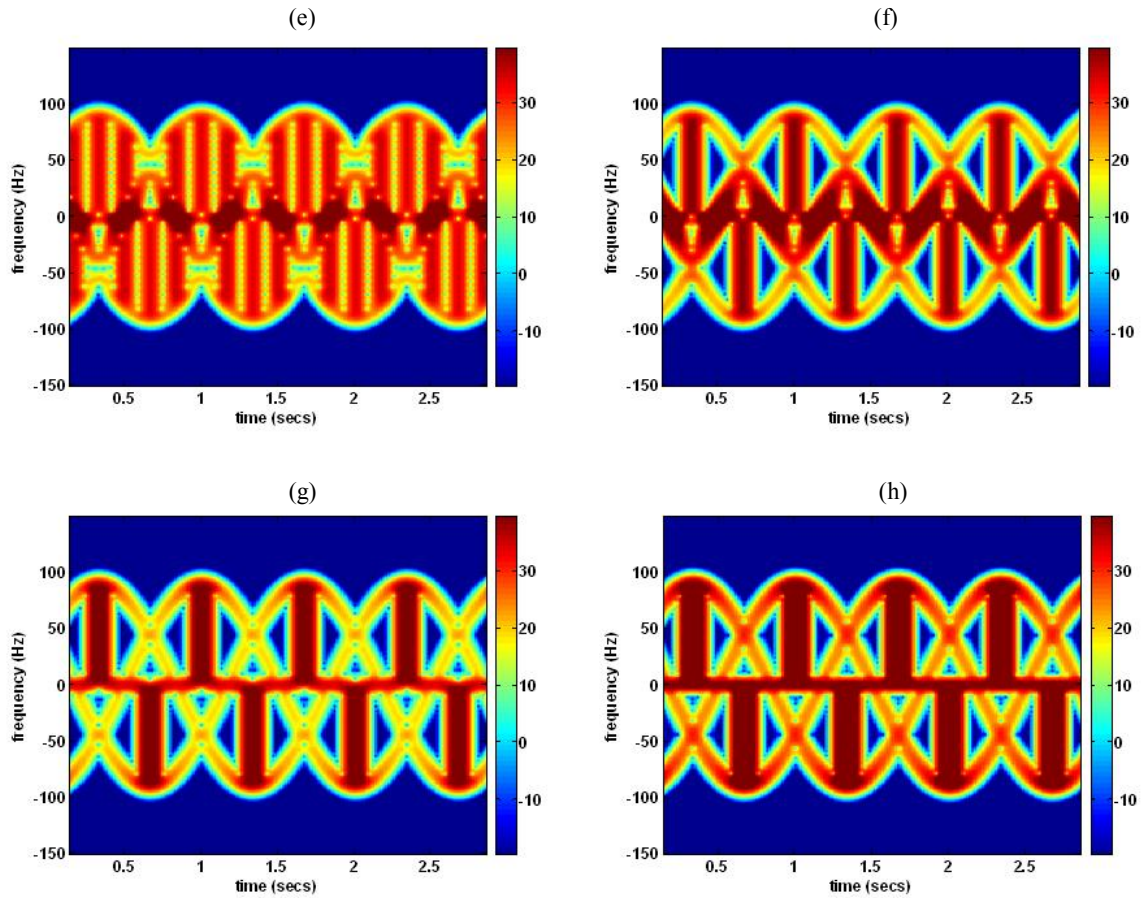


Fig. 3.1. Gradual build up of the turbine using point scatterer model. (a) 3 point particles separated by 120 degrees phase angle (b) $M = 2$; linear spacing between scatterer = 7.5λ (c) $M = 3$; linear spacing between scatterer = 5λ (d) $M = 6$; linear spacing between scatterer = 2.5λ (e) $M = 15$; linear spacing between scatterer = λ (f) $M = 30$; linear spacing between scatterer = 0.5λ (g) $M = 60$; linear spacing between scatterer = 0.25λ (h) $M = 150$; linear spacing between scatterer = 0.1λ .

3.2 Basis Parameterization

As seen in the previous section, the point scatterer model is a very suitable candidate to represent the signal from a turbine and thus, it can be used as a basis to remove the turbine signal. By knowing the correct angular velocity, ω , the starting position, θ , and the strength of the signal of a turbine, the point scatterer basis will give results that closely resemble to the turbine signal. The correct ω and θ values for a signal can be found computationally by searching over a range of ω and θ . The proper strength coefficients are found by first normalizing the basis, then projecting the basis onto the turbine signal. Subtracting the basis from the turbine signal will eliminate the turbine Doppler tracks in the spectrogram. Mathematically, first the basis is normalized as in eq. 4.2, such that the inner product of the normalized basis with itself is 1.

$$\Phi_k'(t) = \frac{\Phi_k(t)}{\sqrt{\langle \Phi_k(t), \Phi_k(t) \rangle}} \quad (\text{eq.3.4})$$

such that,

$$\langle \Phi_k'(t), \Phi_k'(t) \rangle = 1 \quad (\text{eq.3.5})$$

where n represents the basis with a particular ω and θ . Now the turbine signal can be decomposed into the basis function as follows:

$$E(t) = \sum a_k' \Phi_k'(t) \quad (\text{eq.3.6})$$

such that,

$$E(t) = a_1'\phi_1'(t) + a_2'\phi_2'(t) + \dots + a_k'\phi_k'(t) \quad (\text{eq.3.7})$$

Therefore, it follows that:

$$\langle E(t), \phi_1'(t) \rangle = a_1' + a_2' \langle \phi_1'(t), \phi_2'(t) \rangle + \dots + a_k' \langle \phi_1'(t), \phi_k'(t) \rangle \quad (\text{eq. 3.8})$$

where

$$a_1' \cong \langle E(t), \phi_1'(t) \rangle \quad (\text{eq. 3.9})$$

and we assume that the cross terms involving the inner product of the basis with unmatched subscript are small compared to the case when the projection is onto an identical basis function. This method, also known as the adaptive signal parameterization algorithm, searches for the k th basis with maximum projection on the turbine signal [28]. After finding the maximum projection, the basis can be subtracted from the original signal as follows:

$$R(t) = E(t) - a_k'\phi_k' \quad (\text{eq. 3.10})$$

For the next iteration, $E(t)$ is replaced with $R(t)$ and the basis is searched again for matching ω and θ . The next strength coefficient is found in the same manner as described above. The function $R(t)$ is referred to as the residual signal.

3.3 Simulations

The method described above is first applied to the point scatterer generated turbine blades. After validating the applicability of this method on point scatterers, the method is then applied to simulated data from a computational electromagnetics code.

3.3.1 Basis Parameterization Applied to Point Scatterer Data

First, the basis parameterization is applied to a single blade. For the basis function, N in eq. 3.3 is set to 1 which corresponds to a single blade. The spacing between the point scatterers is set at $\lambda/10$, in other words, $M = 150$. Fig. 4.1 (a) shows the original signal generated using point scatterer model. The incident frequency is set to 1GHz, the rotational frequency is 0.5 Hz, and the starting angle is 30 degrees. The y-axis in Fig. 4.1 (b) shows the energy of the signal and the subsequent residuals and the x-axis represents the residual iteration. The energy is defined as:

$$Energy = 10 * \log (\text{sum}(R(t)^2)) \quad (\text{eq. 3.11})$$

where $R(t)$ is the residual signal. At the 0th iteration, $R(t)$ is replaced with the original signal $E(t)$. Thus, the 0th iteration gives the maximum energy in the original signal. It can be seen from Fig. 3.2 that after the first residual iteration, the signal is completely subtracted out and the energy of the signal becomes essentially 0.

In the next test case, an additional blade with equal rotational frequency but with a 90 degree phase angle is inserted into the data. The resulting spectrogram is shown in Fig. 3.3(a). The strength of both blades in this case is identical. Fig. 3.3 (b), (c), and (d) respectively show the spectrogram after the first three residual iterations. From Fig. 3.3 (d), it can be seen that the Doppler tracks are essentially eliminated from the spectrogram and the signal contains very little energy. Moreover, fig 3.4 shows that the energy of the signal becomes non-existent if the process of residual subtraction is continued.

The analysis described above is now performed on two blades with different signal strengths. The signal strength ratio of the blades is 1:100. Fig. 3.5 (a) shows the original signal. Fig. 3.5 (b) and (c), are the 1st and 2nd signals respectively. Finally, Fig.

3.6 shows the energy of the signal as a function of residual subtraction and it can be concluded that this technique is suitable for subtraction of signals with unequal strengths.

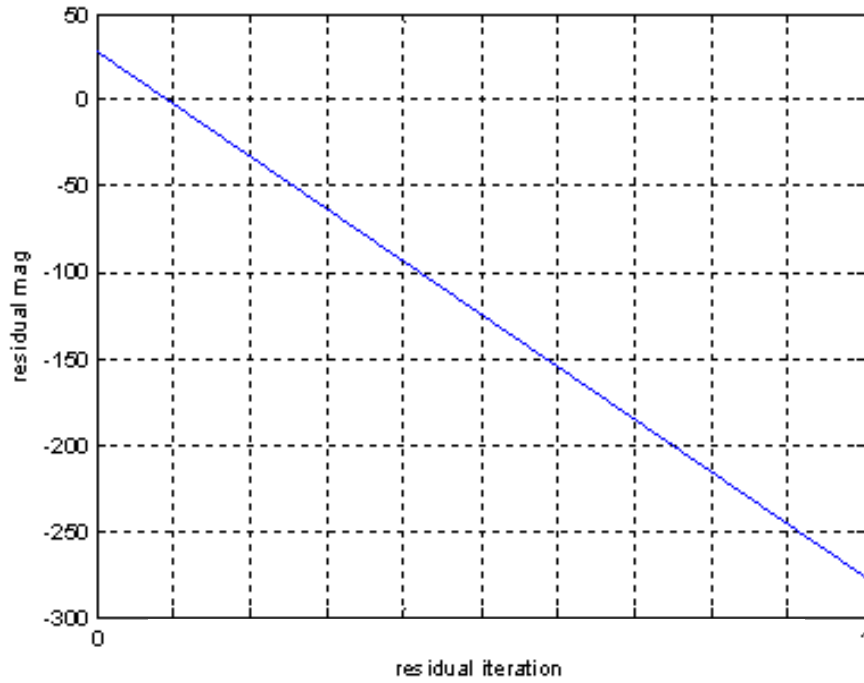


Fig 3.2. Energy of the signal after basis subtraction for a single blade.

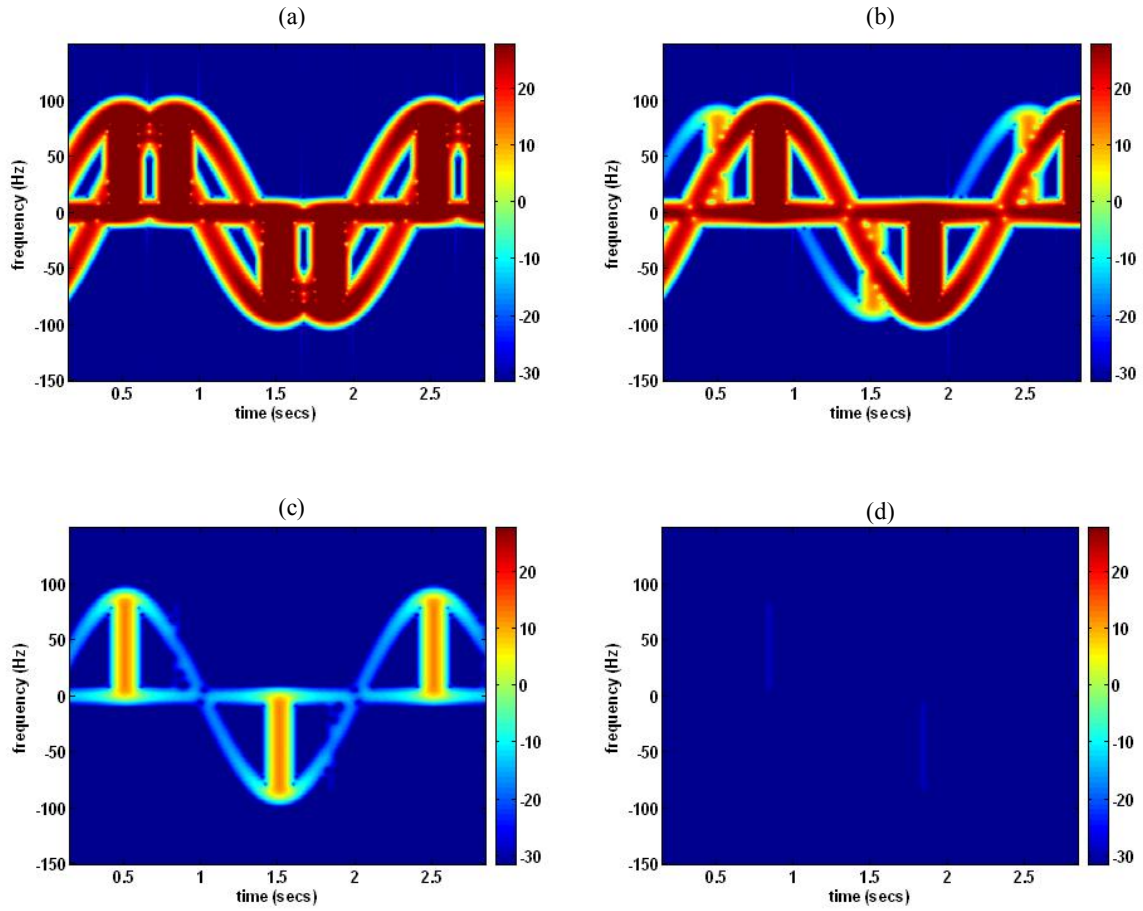


Fig.3.3. Basis parameterization applied on a two single blade of equal strength. (a) Original simulated data (b) spectrogram after 1st residual subtraction (c) spectrogram after 2nd residual subtraction (d) spectrogram after 3rd residual subtraction

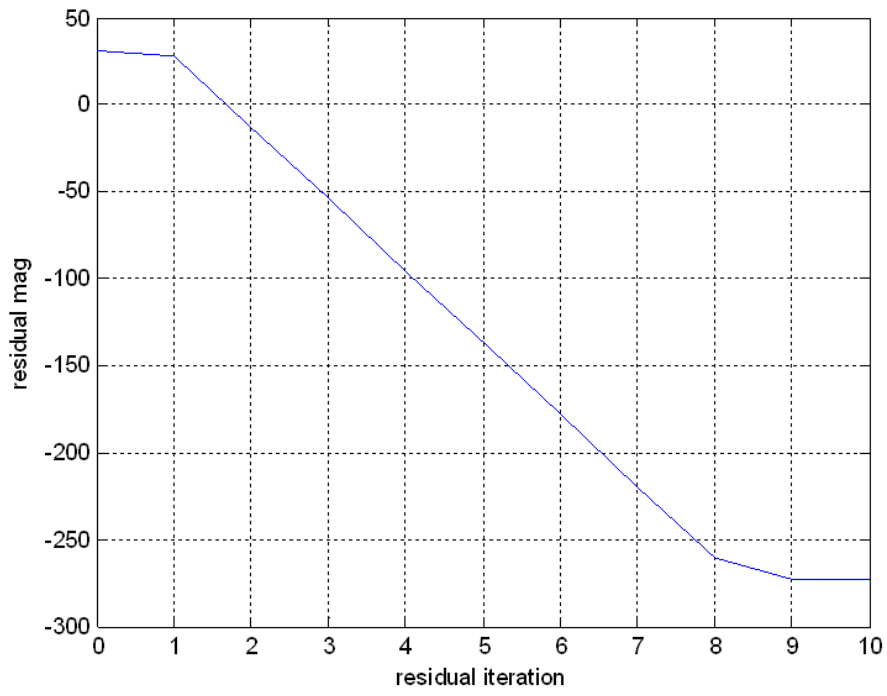


Fig.3.4. Residual energy vs. residual iteration (10 iterations).

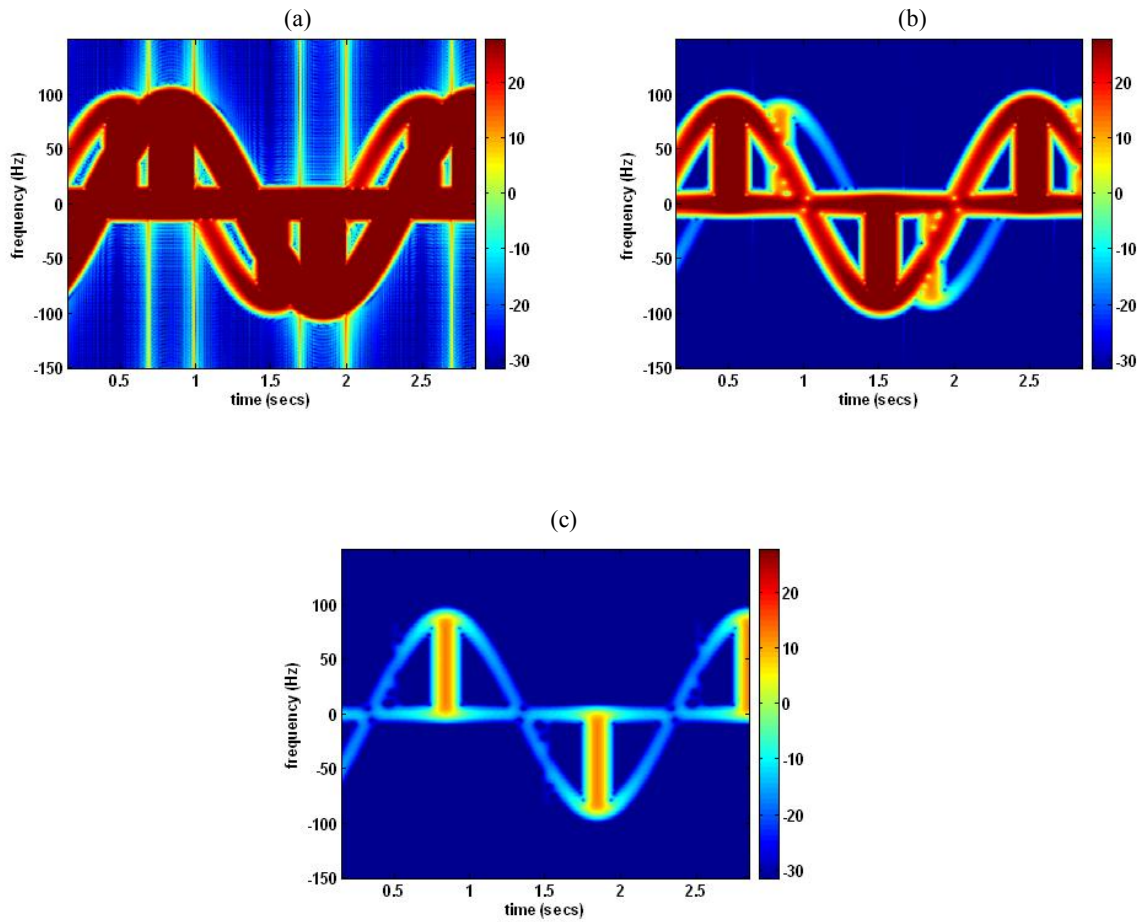


Fig.3.5. Basis parameterization applied on a two single blade of un-equal strength; strength ratio 1:100. (a) Original simulated data (b) spectrogram after 1st residual subtraction (c) spectrogram after 2nd residual subtraction

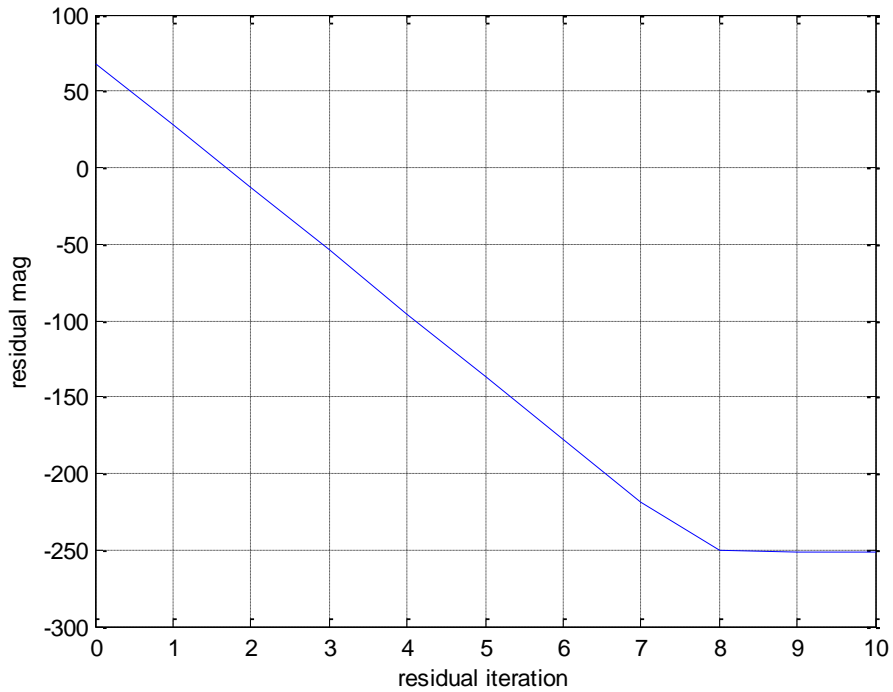
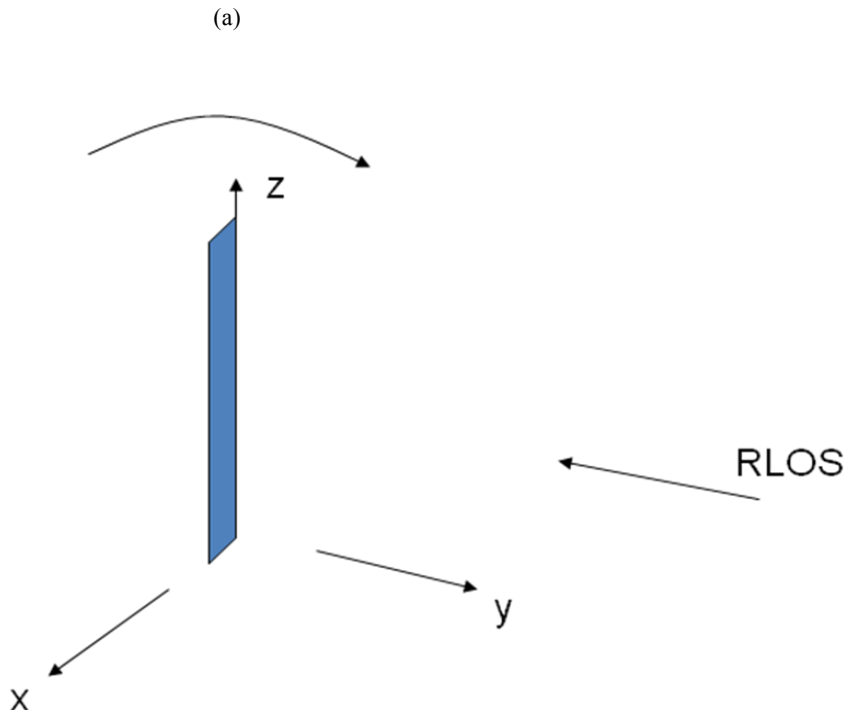


Fig.3.6. Residual energy vs. residual iteration (10 iterations).

3.4.1 Backscattered Data Generated Using Ahilo

In this section, the basis parameterization applied to the point scatterer blades is applied to the data obtained using Ahilo. First, this section presents preliminary simulation results obtained from Ahilo using turbines blades generated from simple CAD models. The size of the blades used is comparable to the blades used in realistic turbines. Ahilo uses the shooting and bouncing ray (SBR) method [29]. Since SBR is used, no multiple interactions resulting from traveling waves are present in the Doppler spectrograms. The first geometry considered is a simple 20 meter long and 1 meter wide rectangular strip shown in Fig.3.7(a). This strip case is analogous to the single blade case analyzed in chapter 2. The strip rotates in left hand sense in the y-z plane and the radar rays are incident on the strip as shown in the figure. Figs. 3.7 (b), (c), (d), and (e) show

the resulting RCS and spectrograms at 0.1GHz and 1GHz. It is observed that RCS has the shape of the sinc function and the peak of the function corresponds to the flashes in the spectrograms. Fig.3.7 (b) and (c) are the RCS and spectrogram at 0.1GHz. The data is sampled at every one degree rotation. The data



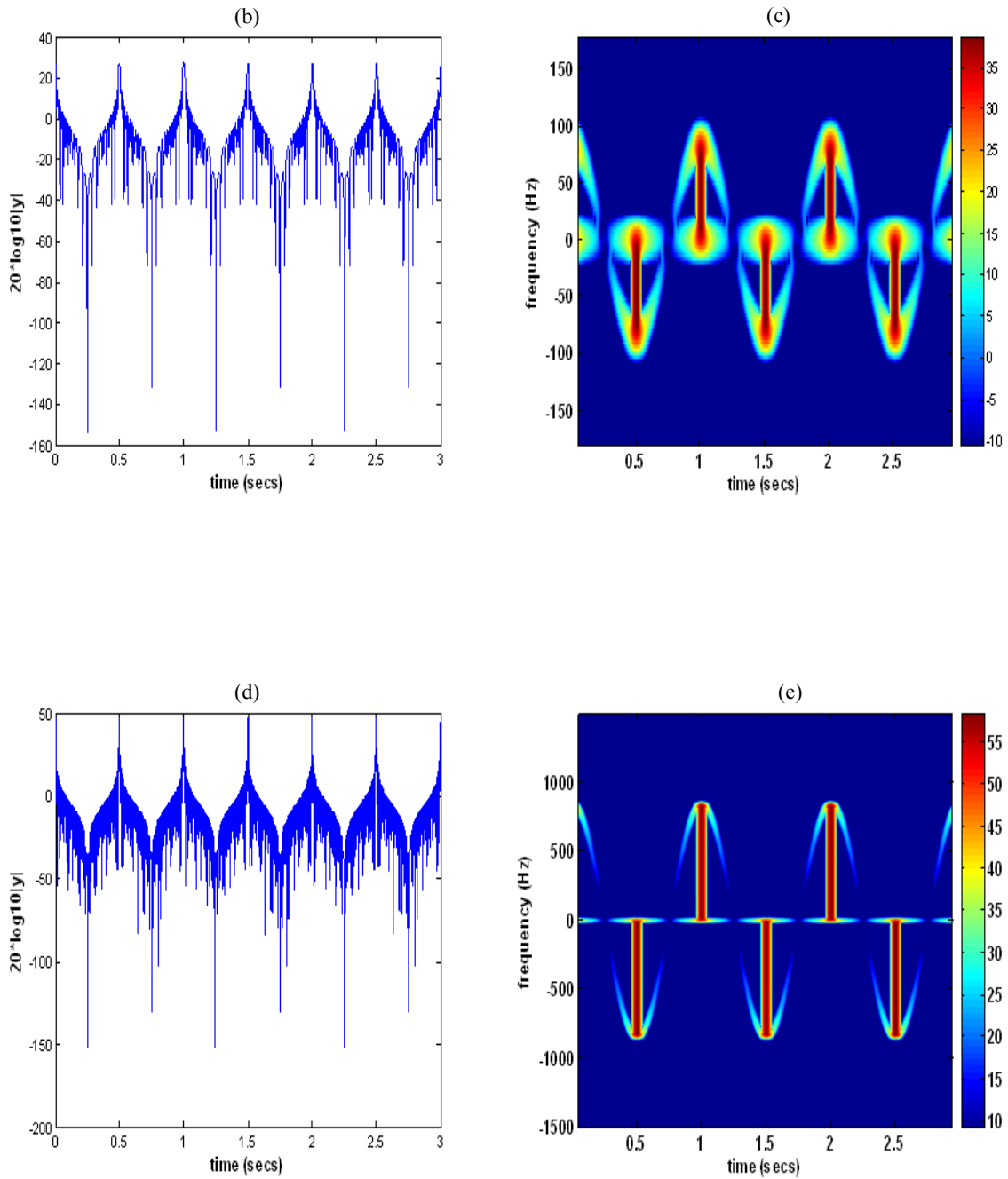


Fig.3.7. Ahilo results for a rectangular strip. (a) Strip geometry. (b) RCS at 0.1GHz. (c) spectrogram at 0.1GHz. (d) RCS at 1GHz. (e) spectrogram at 1 GHz.

shown in Fig.3.7 (d) and (e) is sampled finer--every 0.12 degrees-- due to the higher incident frequency. Fig. 3.8 shows the results for three rectangular strips used to model three blades of turbine.

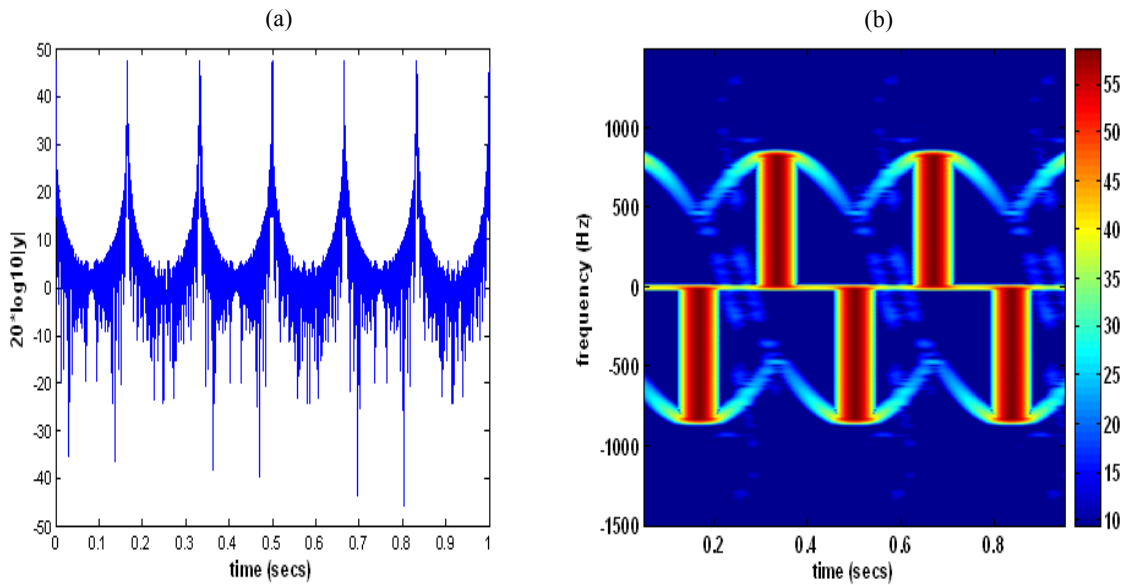


Fig.3.8. Ahilo results for a three rectangular strip. (a) RCS at 1GHz. (b) spectrogram at 1 GHz.

3.4.1 Basis Parameterization Applied to Ahilo data

A single strip run result obtained from Ahilo is shown in Fig. 3.9 (a). The incident frequency is set to 1GHz, the frequency of rotation of the strip is 0.99967 and the starting angle is 0 degrees. For the basis function, as in the previous section, N in (eq. 3.3) is set to 1. The spacing between the point scatterers in the basis function is $\lambda/10$. With the same parameters as those used to generate the Ahilo results, the point scatterer basis' time-frequency characteristics look as shown in Fig. 3.9 (b).

The Ahilo signal is parameterized in the same manner as described earlier and the result of the first residual are shown in Fig. 3.10. From Fig. 3.10 (c), it can be seen that the signal is not completely subtracted as was the case with a single blade run in the previous section. This can be explained by the gaps seen in the Ahilo spectrogram at 0.25 and 0.75 seconds. At these two instances, the strip in Fig. 3.7 (a) is parallel to the RLOS and therefore, perpendicular to the direction of the incident electric field. Therefore, no current is induced in the strip. However, the point scatterer basis fails to take this effect into account. Hence, the original signal is not completely subtracted. Since the first residual no longer resembles the basis function, which is due to the basis being an approximation of the real signal, the subsequent residuals will not completely be eliminated as can be seen in Fig. 3.10. Fig. 3.10(a), (b), and (c) show the spectrogram after the 1st, 2nd, and 3rd residual subtraction. Therefore, the basis used can be suitably used to eliminate the dominant tracks in the spectrogram. Fig. 3.11 shows the residual energy of the signal as a function of residual iteration. It is clear that after a large reduction in the energy of the signal after the first 2 iterations, the basis is not successful in reducing energy of the signal by a significant amount as the number of iteration increases. The basis needs to be modified in order to completely remove the Doppler tracks from the Ahilo data. However, it is successful at removing a large and most dominant part of the turbine signal.

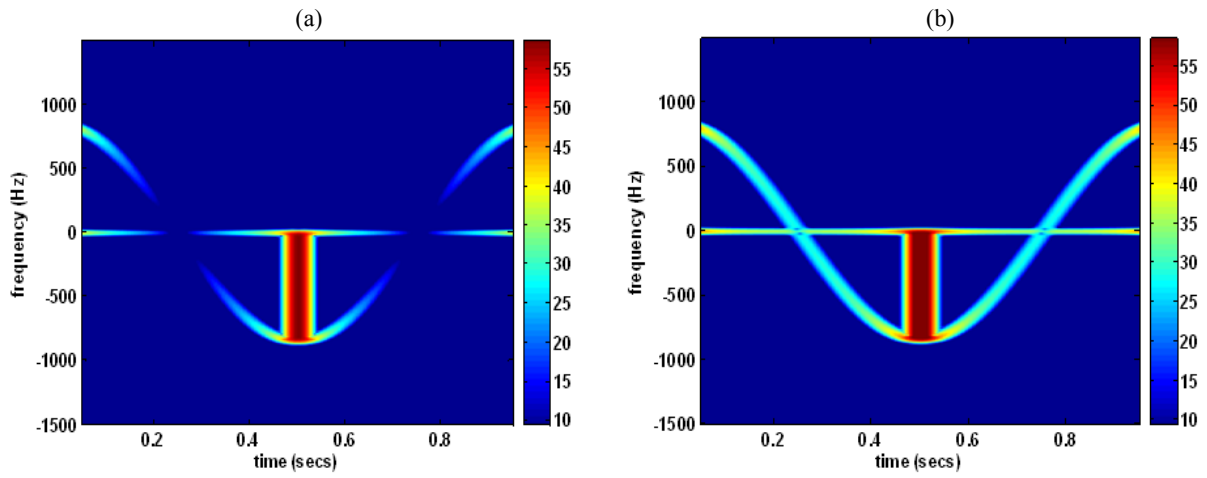


Fig.3.9. Single blade simulation (a) Ahilo (b) point scatterer basis with $\lambda/10$ spacing between point scatterers.

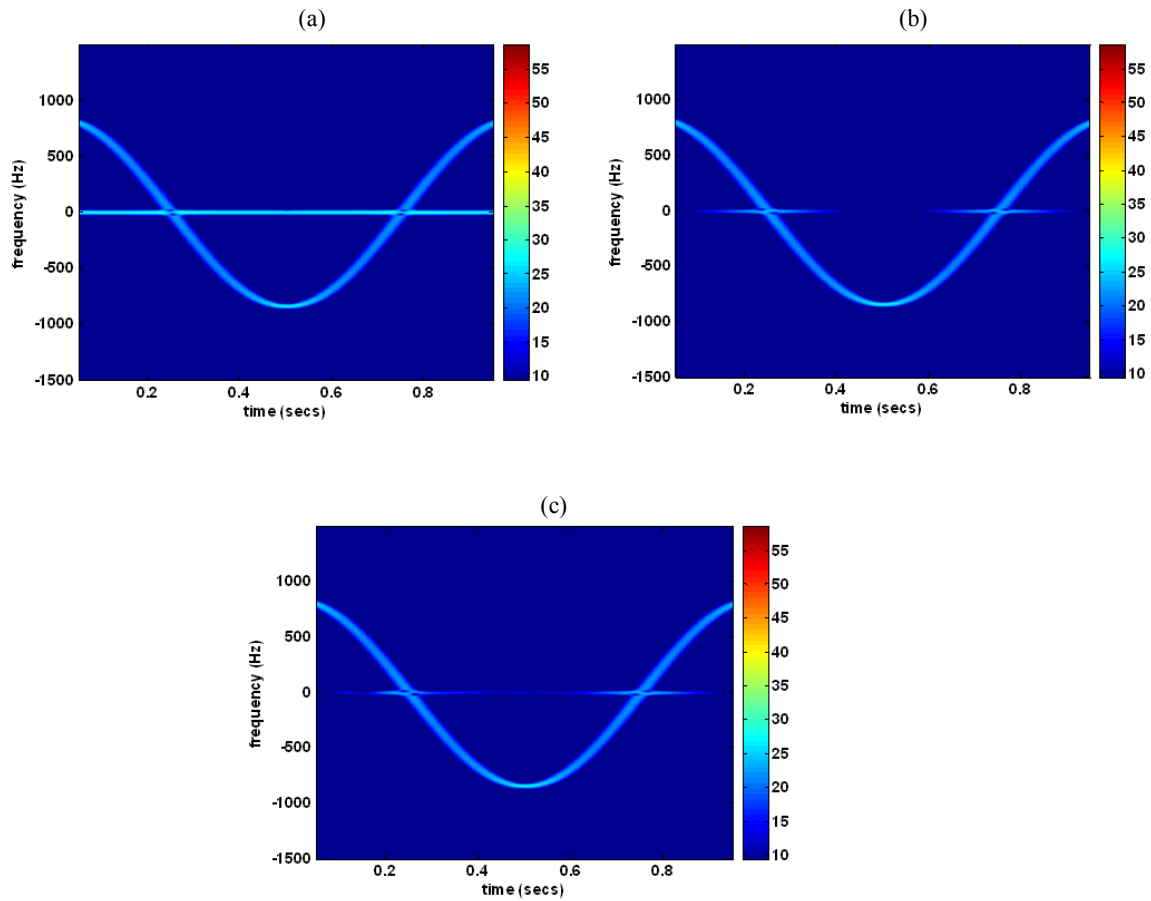


Fig.3.10. Basis parameterization applied on Ahilo data. (a) spectrogram after 1st residual subtraction (b) spectrogram after 2nd residual subtraction (c) spectrogram after 3rd residual subtraction.

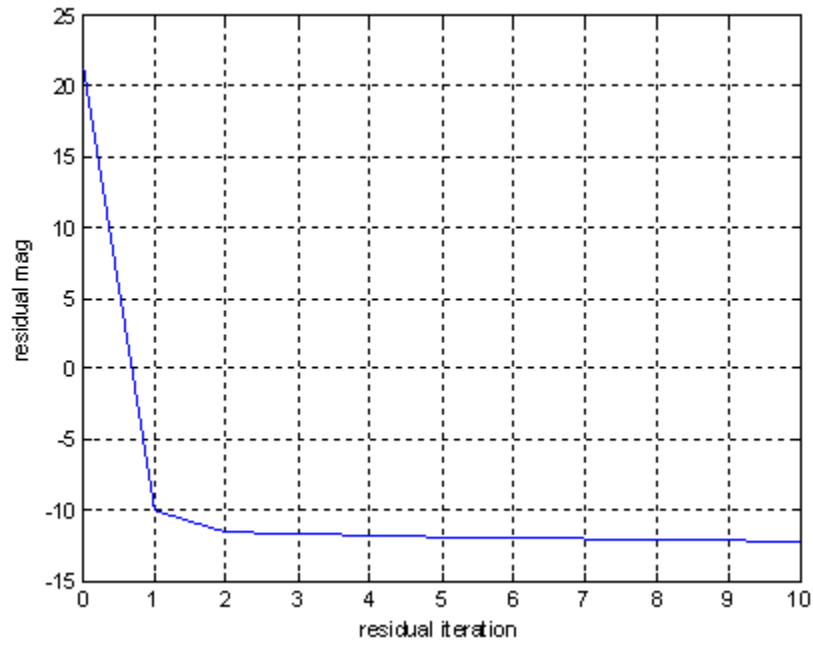


Fig. 3.11. Residual energy vs. residual iteration on Ahilo data(10 iterations).

Chapter 4

Conclusions

This thesis first investigated the radar scattering from three different wind turbine models. Dynamic CW radar measurements were performed in the laboratory and the resulting data were analyzed using the short-time Fourier transform to study their Doppler scattering features. For the 1:160 scaled model turbine, it was found that our measurements captured the gross Doppler features including blade flashes and tip halos observed in a large wind turbine reported in [11-15]. For the 3-arm wire model, additional multiple scattering and near field effects were observed and interpreted with the aid of simulations performed using NEC. It was also found that only multiple scattering gives rise to non-zero forward Doppler. For the Bergey Windpower turbine, we observed unequally spaced, curved flashes. They are attributable to the unique shape of the turbine blade.

Second, a filtering algorithm to parameterize the signal into basis functions was developed and successfully applied to completely eliminate the signal energy of the simulated point scatterer data. This algorithm was next applied to some preliminary results generated using the Ahilo software and the dominant signal features were successfully removed.

Future work will improve this filtering algorithm to take account of a moving target in addition to the wind turbines in the signal. The arbitrary motion of the moving target will be parameterized by a chirplet basis discussed in [30]. Moreover, the algorithm will be enhanced to subtract the received signal from wind turbines in real time.

Bibliography

- [1] D. L. Sengupta and T. B. A. Senior, "Electromagnetic Interference to Television Reception Caused by Horizontal Axis Windmills," *Proc. IEEE*, vol. 67, pp. 1133-1142, Aug. 1979.
- [2] D. L. Sengupta and T. B. A. Senior, "Electromagnetic Interference from Wind Turbines," in *Wind Turbine Technology*, D. A. Spera, New York: ASME Press, 1994, pp. 447-486.
- [3] C. Salema and C. Fernandes, "Co-Sitting Criteria for Wind Turbine Generators and Transmitter Antennas," *Proc. Confielle 1999 – II Conf. de Telecomunicacoes*, Sesimbra, Portugal, pp. 466-470, 1999.
- [4] C. Salema, C. Fernandes, and L. Fauro, "TV Interference from Wind Turbines," *Proc. 3rd Conference on Telecommunications*, Figueira da Foz, Portugal, pp. 47-51, 2001.
- [5] *Special Evaluation Report to Assess Effect of Wind Turbine Farm on Air Route Surveillance Radar-4 at King Mountain, Texas*, USAF 84 RADES & FAA, May 30, 2002.
- [6] G. J. Poupart, "Wind Farms Impact on Radar Aviation Interests," QinetiQ Corp., Final Report to the Dept. of Trade and Industry, UK, Sept. 2003.
- [7] *The Effects of Wind Turbine Farms on ATC RADARS*, Air Warfare Center, Royal Air Force, UK, May 10, 2005.
- [8] *Further Evidence of the Effects of Wind Turbine Farms on AD RADARS*, Air Warfare Center, Royal Air Force, UK, Aug. 12, 2005.

- [9] M. Brenner, "Wind Farm and Radar," The MITRE Corp., Report JSR-08-125 to the Dept. of Homeland Security, Jan. 2008.
- [10] *Report of the Effect on Radar Performance of the Proposed Cape Wind Project and Advance Copy of USCG Findings and Mitigation*, U. S. Department of the Interior Minerals Management Service, Jan. 2009.
- [11] *The Effect of Windmills on Military Readiness*, United States Department of Defense Report to the Congressional Defense Committees, 2006.
- [12] B. M. Kent, K. C. Hill, A. Buterbauch, G. Zelinski, R. Hawley, L. Cravens, T. Van, C. Vogel, and T. Coveyou, "Dynamic Radar Cross Section and Radar Doppler Measurements of Commercial General Electric Windmill Power Turbines," *IEEE Antennas Propagat. Mag.*, vol. 50, pp. 211-219, Apr. 2008.
- [13] B. M. Kent, A. Buterbaugh, K. C. Hill, G. Zelinski, R. Hawley, L. Cravens, T. Van, C. Vogel, and T. Coveyou, "Dynamic Radar Cross Section and Radar Doppler Measurements of Commercial General Electric Windmill Power Turbines Part 2 – Predicted and Measured Doppler Signatures," *Proc. 2007 AMTA Symposium*, St. Louis, MO, 2007.
- [14] K. C. Hill, G. Zelinski, T. Van, and C. Vogel, "Computational Electromagnetics (CEM) Prediction of a Windmill," *2007 Electromagnetics Code Consortium Annual Meeting*, May 2007.
- [15] *The Air Force Research Laboratory (AFRL) Mobile Diagnostics Laboratory (MDL) Wind Farm Turbine Measurements Fenner, NY*, Final Report, July 2006.
- [16] A. Huuskonen, "OPERA Final Report," Finnish Meteor. Inst., Mar. 2007.
- [17] D. W. Burgess, T. Crum, and R. J. Vogt, "Impacts of Wind Farms on WSR-88D Operations," *24th Int. Conf. on Interactive Information Processing Systems (IIPS)*

for Meteorology, Oceanography, and Hydrology, Amer. Meteor. Soc., Paper 6B.3, New Orleans, LA, 2008.

- [18] J. B. Sandifer, T. Crum, E. Ciardi, and R. Guenther, "A Way Forward: Wind Farm Weather Radar Coexistence," WINDPOWER 2009, Chicago, IL, May 2009.
- [19] H. E. Green, "Electromagnetic Backscattering from a Helicopter Rotor in the Decametric Wave Band Regime," *IEEE Trans. Antennas Propagat.*, vol. 42, pp. 501-509, Apr. 1994.
- [20] R. Bhalla and H. Ling, "A Fast Algorithm For Simulating Doppler Spectra of Targets With Rotating Parts Using the Shooting and Bouncing Ray Technique," *IEEE Trans. Antennas Propagat.*, vol. 46, pp. 1389-1391, Sept. 1998.
- [21] T. Thayaparan, S. Abrol, E. Riseborough, L. Stankovic, D. Lamothe, and G. Duff, "Analysis of Radar Micro-Doppler Signatures from Experimental Helicopter and Human Data," *IET Proc. Radar Sonar Navigat.*, vol. 1, pp. 289-299, Aug. 2007.
- [22] B. M. Isom, R. D. Palmer, G. S. Secrest, R. D. Rhoton, D. Saxion, T. L. Allmon, J. Reed, T. Crum, and R. Vogt, "Detailed Observations of Wind Turbine Clutter with Scanning Weather Radars," *Journal of Atmospheric and Oceanic Technology*, vol. 26, pp. 894-910, May 2009.
- [23] M. M. Butler and D. A. Johnson, "Feasibility of Mitigating the Effects of Windfarms on Primary Radar," Alenia Marconi Systems Limited, 2003.
- [24] A. Tennant and B. Chambers, "Radar Signature Control of Wind Turbine Generators," *IEEE Antennas Propagat. Soc. Int. Symp.*, pp. 489-492, Washington, DC, July 2005.
- [25] A. Tennant and B. Chambers, "Signature Management of Radar Returns from Wind Turbine Generators," *Smart Materials Structures*, vol. 15, pp. 468-472, Feb. 2006.

- [26] J. C. G. Matthews, J. Pinto, and C. Sarno, "Stealth Solutions to Solve the Radar-Wind Farm Interaction Problem," *2007 Loughborough Antennas Propagat. Conf.*, pp. 101-104, Loughborough, UK, Apr. 2007.
- [27] Y. Wang, H. Ling, and V. C. Chen, "Application of Adaptive Joint Time-Frequency Processing to ISAR Image Enhancement and Doppler Feature Extraction for Targets with Rotating Parts," *Proc. SPIE-Int. Soc. Optic. Eng.*, vol. 3462, pp. 156-163, 1998.
- [28] V. C. Chen and H. Ling, *Time-Frequency Transforms for Radar Imaging and Signal Analysis*, Massachusetts: Artech House, 2002.
- [29] H. Ling, R. C. Chou, and S. W. Lee, "Shooting and Bouncing Rays: Calculating the RCS of an Arbitrarily Shaped Cavity," *IEEE Trans. Antennas Propagat.*, vol. 37, pp. 194-205, Feb. 1989.
- [30] J. Li and H. Ling, "Application of Adaptive Chirplet Representation for ISAR Feature Extraction from Targets with Rotating Parts," *IEE Proc.-Radar Sonar Navigat.*, vol. 150, pp. 284-291, Aug. 2003.

Vita

Aale Naqvi graduated with a B.Sc in Physics from University of Texas at Arlington in 2004. He is currently pursuing his PhD in Electrical Engineering at University of Texas at Austin.

Permanent address: 809 Cherry Laurel Lane, Arlington, TX. 76012

This thesis was typed by the author.